Effect of Nitridation on High Temperature Corrosion of Ferritic Stainless Steel

by

Tiziano Bergamo

Diploma work No. 107/2013
at Department of Materials and Manufacturing Technology
CHALMERS UNIVERSITY OF TECHNOLOGY
Göteborg, Sweden

Performed at: Department of Materials and Manufacturing Technology
Chalmers University of Technology
SE-412 96 Göteborg

Supervisor(s): Univ. Lec. Mats Norell
Dr. Emmy Yu Cao
Department of Materials and Manufacturing Technology
Chalmers University of Technology
SE-412 96 Göteborg

Examiner: Univ. Lec. Mats Norell
Department of Materials and Manufacturing Technology
Chalmers University of Technology
SE-412 96 Göteborg

Effect of Nitridation on High Temperature Corrosion of Ferritic Stainless Steel
TIZIANO BERGAMO

Diploma work No. 107/2013
Department of Materials and Manufacturing Technology
Chalmers University of Technology
SE-412 96 Göteborg
Sweden

Reproservice
Göteborg, Sweden 2013

Effect of Nitridation on High Temperature Corrosion
of Ferritic Stainless Steel
TIZIANO BERGAMO
Department of Materials and Manufacturing Technology
Chalmers University of Technology

Abstract

The emission of nitrogen monoxide in the atmosphere is one of the main causes of air pollution. In this regards, the truck industry introduced the Selective Catalytic Reduction (SCR) in exhaust after-treatment system of heavy-duty trucks. Through the use of urea water solution injected into the gas flow, NOx can be reduced to N_2 and H_2O. The high temperatures in the exhaust system, together with the products of the reduction reactions, produce a particularly corrosive environment, strongly detrimental for the corrosion resistance of the stainless steels used.

The aim of this work was to evaluate the effect of nitridation on the oxidation resistance of AISI 444 ferritic stainless steel. The oxidation of both as-received and nitrided 444 coupons in the presence of 10% H_2O was investigated in the temperature range of 450 and 600°C. The exposure time was between 24 and 168 hours. The samples were characterized by using several techniques including LOM, SEM, EDS, XPS, XRD. An expanded ferrite phase supersaturated with nitrogen was formed on the surface of 444 ferritic stainless steel after plasma nitriding at about 400°C. The layer thicknesses were about 10-20 µm with a nitrogen atomic content of about 15-13%. The detrimental effect of nitridation was very strong on the oxidation resistance of ferritic 444. The oxide scales formed on nitrided samples were 50-100 times thicker than on as-received samples. The lower chromium activity in nitrided 444 due to formation of short-range ordering with nitrogen decreases the chromium diffusion toward the surface and hinders formation of protective oxides. The oxidation on 444 ferritic stainless steel definitely decreased with increasing temperatures, although the larger formation of Cr-nitrides at higher temperatures. The increase of chromium diffusion due both to higher temperatures and larger leak of nitrogen from the expanded ferritic phase improves the oxidation resistance of the ferritic 444. The oxidation resistance in presence of 10% H_2O at 450-600°C seems better for nitrided 444 ferritic stainless steel than for nitrided 304L austenitic stainless steel investigated in previous studies.

Keywords**:** Selective Catalytic Reduction (SCR); Ferritic Stainless Steel; Plasma Nitriding; Expanded Phase; High Temperature Oxidation; Water Vapor; LOM; SEM; EDS; XPS; XRD.

Preface

This master degree project has been carried out from September 2012 to February 2013 at the Department of Materials and Manufacturing Technology at Chalmers University of Technology. The work has been performed within the HTC-project “High Temperature Corrosion in Diesel Exhaust Gas After-Treatment Systems” in co-operation with Volvo Powertrain and Outokumpu Stainless.

At the end of this work I would like to thank particularly my supervisor Dr. Emmy Yu Cao and my supervisor and examiner Dr. Mats Norell for their precious help and support during the entire project.

I would also like to thank Prof. Lars Nyborg for giving me the opportunity to perform my thesis here, at Chalmers University of Technology.

Finally, I would like to thank all the people working at the department, who have helped me during these six months, especially Urban Jelvestam for his help with XPS analyses and Yiming Yao for her help with the use of SEM and EDS analyses.

Göteborg, March 2013

Tiziano Bergamo

Contents

Chapter 1

Introduction

1.1 Background

Pollution is a problem we are inevitably faced with. Accordingly, many countries have enacted special laws to lower the polluting emissions of fossil fuel. The emission of nitrogen monoxide in the atmosphere is one of the main causes of air pollution. Nitrogen monoxide, when dissolved in atmospheric moisture, can form particulates and nitric acid, a component of acid rain. By sunlight it can react with volatile organic compounds forming ozone at ground level, which is particularly harmful to the health. Furthermore, it is connected to the enlargement of the ozone hole and contributes to the greenhouse effect.

The major source of NOx production derives definitely from the exhaust gas of vehicles. For this reason, many systems have been developed over the years in order to lower the content of this pollutant. For this purpose the truck industry chose the Selective Catalytic Reduction (SCR) system. By catalyzing NOx content in exhaust gases with the reduction agent ammonia (NH_3), which is added in diesel exhaust system in the form of urea water solution, NOx content is considerably reduced. Such reaction generates water and nitrogen that can be easily emitted.

The use of urea within the diesel exhaust after-treatment systems involves some problems related with corrosion resistance of the materials. The high temperatures in the exhaust system, together with the products of the reduction reaction, produce a particularly corrosive environment, which complicates the choice of the material used. Studies have been done to select which material was characterized by the best price-quality ratio for this application. Concerning this, the use of stainless steels was found to be a possible choice. The good strength combined with the good corrosion resistance at low and high temperatures make them particularly suitable for this application. Nevertheless, the reaction between urea and NOx leads to the absorption of nitrogen present as a reaction product. Both the formation of expanded phases supersaturated with nitrogen and the precipitation of chromium nitrides at higher temperatures leads to a decrease of the chromium activity. Also the presence of water vapor within the exhaust after-treatment system decreases the oxidation resistance of the stainless steels because of the vaporization of volatile chromium species from the protective chromium-oxide scale, which changes in non-protective iron-oxide scale.

1.2 Aim of Research

The purpose of this study is to evaluate the effect of nitrogen uptake on high temperature corrosion of ferritic stainless steel. This work focuses on the degradation of the AISI 444 ferritic stainless steel in view of possible uses in urea-SCR systems. The material has been studied by exposing both as-received and nitrided coupons in presence of humid air containing 10% H_2O at the temperature

range 450 to 600°C. Analyses of morphology, thickness and atomic composition of the oxide layer have been carried out through the use of several techniques, including LOM, SEM, EDS, XRD, XPS.

1.3 Delimitations

Since this project has a timeframe of 6 months, a reduction of the research field is necessary. For that, the following delimitations have been set up:

- The alloy analyzed during this work is the 444 ferritic stainless steel. References and comparisons between this and others austenitic grades have been possible thanks to previous works.
- Kinetic of oxide growth at different temperatures for the 444 ferritic stainless steel has not been studied by using thermogravimetry in this work.
- External partner performed plasma nitriding process on the plates of 444 ferritic stainless steel.

Chapter 2

Literature Review

2.1 Selective Catalytic Reduction (SCR) System

The urea selective catalytic reduction is one of the most important techniques used to reduce nitrogen oxide (NOx) emissions. Schematic of SCR system is shown in **Figure 1**. Urea is a solid compound for ammonia, which is the reducing agent that directly reacts with NOx on a catalyst surface.

For applications in mobile diesel engines the directly use of ammonia is not possible, since storage and transport would be complicated and dangerous. The problem was solved by using a water solution of urea (32.5% by weight [1]), stored in a tank on the outside of the truck beside the diesel tank. Firstly, the urea solution is pumped in a dosing unit and then is sprayed through a nozzle into the exhaust flow, just before the muffler. The temperatures inside the exhaust flow can reach 250-600°C, depending on the engine workload. Below 250°C the catalyst does not work [2]. For this reason no urea is used as the engine heats up.

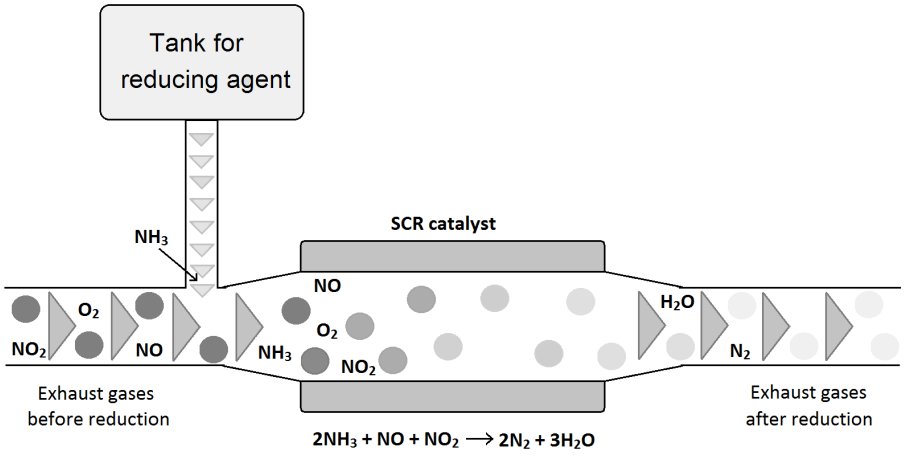

Figure 1. Model of the SCR system.

2.1.1 Main SCR Reactions with Ammonia

When the urea solution is sprayed into the exhaust flow, water is vaporized and the urea starts to decompose. It is generally accepted that urea decomposes in two different steps [3]. Firstly there is the thermolysis of the urea molecules into ammonia and isocyanic acid:

$$(NH_2)_2CO \rightarrow NH_3 + HCNO$$

which occurs within the exhaust pipe, before the catalyst, and then there is the hydrolysis of isocyanic acid, which occurs on the catalyst surface and leads to the formation of ammonia and carbon dioxide:

$$HNCO + H_2O \rightarrow NH_3 + CO_2$$

According to the two reactions above, each mole of urea generates two mole of ammonia, that directly react with NO or NO_2 on the catalytic surface. The two main SCR reactions between ammonia and NOx are shown below [3]:

$$4NH_3 + 4NO + O_2 \rightarrow 4N_2 + 6H_2O \quad \text{(standard SCR)}$$

$$4NH_3 + 2NO_2 + 2NO \rightarrow 4N_2 + 6H_2O \quad \text{(fast SCR)}$$

The presence of O_2 molecules in the standard SCR reaction is needed to re-oxidize the catalyst surface. The NO_2 molecules play a similar role in the fast SCR reaction. The faster reaction suggests that NO_2 can re-oxidize the catalyst faster than O_2.

Previously the desirable reactions that occur in a SCR system are reported. In addition to these, there are other undesirable reactions. These reactions do not lead to a lowering of the NOx content in the exhaust gases and also are detrimental for the system. For example, the oxidation of NH_3 with oxygen should be removed, since it not only consume ammonia required for SCR process but also generate NOx. Other undesirable reactions are sulfation and nitration of NH_3. Ammonia can react with SO_2 or NO_2 when there is water and the temperature is low. Anyway, the concentration of SO_2 and NO_2 in exhaust gases is much smaller than the urea concentration, so the loss of ammonia due to the formation of NH_4NO_3 and $(NH_4)_2SO_4$ can be ignored. The major losses of urea are due to the polymerization reactions, which occur during urea decomposition and can lead to the formation of polymers such as polymeric melamine [3].

2.1.2 Problem of Urea Corrosion

The use of urea within the diesel exhaust after-treatment systems in addition to the high temperatures reached generates a particular detrimental environment in the corrosion point of view. Although the urea has been used for some years in stationary combustion plants, not many investigations regarding the influence of urea on corrosion in diesel exhaust system can be found. The majority of articles related to urea corrosion refer to the fertilizer production industry. Although the operating conditions in these plants are far from those found in exhaust after-treatment systems, a quick survey could be in any case useful to understand the corrosion behavior in these environments.

Urea is produced at high pressure and at temperatures in the range of 200°C [4]. The two basic raw materials used are liquid ammonia (NH_3) and gaseous carbon dioxide (CO_2). The reaction takes place in two steps, since carbonic acid does not form a stable ammonium salt. The reaction between ammonia and CO_2 has to be carried out under high temperature and pressure to form the

intermediate product ammonium carbamate. This compound which is the most corrosive species is formed only at high pressures, so it is not present in the exhaust system.

2.2 Stainless Steels

Stainless steels are iron-base alloys with a minimum of 11.5% chromium content by weight [5]. Chromium content increases the oxidation and corrosion resistance of steel in aggressive environments and prevents the formation of rust. The corrosion resistance is provided by a thin surface film, known as “passive film”, which protects the underlying material. The chromium content of 11.5% by weight is the minimum quantity necessary for a continuous layer [6]. Upon increasing the chromium content, the passive layer becomes more stable. The best protections are reached with 25 to 30% chromium content in the non-nickel alloys, and 18-30% in the nickel austenitic alloys [5].

This thin surface film which enables the high resistance to oxidation of stainless steels is generally a chromic oxide film, Cr_2O_3. This oxide is usually not pure chromic oxide and can contain small amounts of iron, manganese and nickel, too. The growth rate of the oxide film is very slow, since the control mechanism of its formation is thought to be the diffusion of cations through it. Lower-chromium stainless steels typically form the spinel oxide $FeCr_2O_4$ that under certain conditions turns out to be also relatively protective. However, the most protective situation occurs with the formation and maintenance of Cr_2O_3 [6].

Today a large number of different alloys belonging to the stainless steel group are present on the market. They differ in the amount of chromium, that in some alloys reaches 30% and in the content of the other alloying elements, added to provide specific properties. For example, nickel and molybdenum are typically added to increase the corrosion resistance of the alloy, expanding the passivity ranges and reducing pitting [5-6]. Carbon, molybdenum, nitrogen, titanium, aluminum and copper are used to increase the strength while sulfur and selenium to facilitate the machinability [6]. Nickel is also added in order to improve the formability and toughness of the material [6].

2.2.1 Families of Stainless Steels

The most common stainless steels can be divided into five major families according to crystallographic structure: ferritic, austenitic, martensitic, duplex and precipitation-hardening [7]. Each family has its typical mechanical properties and is characterized by a common nature in terms of resistance to particular forms of corrosion.

2.2.1.1 Ferritic Stainless Steels

Ferritic stainless steels are alloys of iron and chromium (17 to 27% by weight [5]), with a relatively low carbon content (<0.08%). Chromium is a ferrite stabilizer, therefore a greater chromium content increases its stability [7]. The ferrite is magnetic, and is characterized by body-centered cubic (BCC) crystal structure [5]. Typically, ferritic stainless steels have better engineering properties than austenitic grades, but reduced corrosion resistance. They are highly resistant and in some cases immune to chloride stress-corrosion cracking (SCC). Ferritic stainless steels are typically less expensive than the austenitic grades, because of the very low nickel content. Some alloys may contain a small amount of molybdenum, aluminum, silicon and manganese too [6].

2.2.1.2 Austenitic Stainless Steels

Austenitic stainless steels are the most common of the stainless grades. They are basically alloys of iron, chromium (16 to 27% by weight), and nickel (6 to 22% by weight) [5]. Austenitic stainless steels are particularly resistant to corrosion and oxidation at high temperatures. Austenite, with face-centered cubic (FCC) crystal structure, is nonmagnetic, has relatively low yield strength, high ductility, rapid work hardening rates and excellent toughness [7]. The austenitic stainless steels are typically classified in two series, the AISI 300 and the AISI 200.

The 300 series represents the largest category of stainless steels produced in the United States. These alloys are known as nickel stainless steels because of the large amount of nickel content, required to stabilize the austenitic phase at room temperature. The chemical composition of the alloys can be modified to increase the corrosion resistance. Molybdenum or molybdenum plus nitrogen are added to improve the pitting and crevice corrosion resistance. The carbon content is kept low and the alloy is stabilized with titanium or niobium plus tantalum to reduce intergranular corrosion in welded materials. Nickel and chromium are added to improve high-temperature oxidation resistance and strength. Nickel is added to improve stress corrosion resistance too [6].

The 200 series groups the nickel-manganese-nitrogen stainless steels. These steels were introduced to limit or remove the content of the expensive nickel, in favor of other austenite stabilizers such as carbon, nitrogen, manganese, copper and cobalt. None of these elements alone suffices to obtain a good austenitic stainless steel. The only two nickel-free manganese alloys are Tenelon and 18-18 Plus. In these cases there is large manganese content, about 18%, and significant amount of the other austenite stabilizers [6].

2.2.1.3 Martensitic Stainless Steels

The martensitic stainless steels are not as corrosion resistant as the ferritic and austenitic, but they are extremely strong and tough and can be hardened by heat treatment. The crystal structure is a body-centered tetragonal structure (BCT). They have lower chromium levels (11.5 to 17 by weight [5]) and relatively high carbon contents. The chromium content must be low because of its ferrite-stabilizing character. For this reason the corrosion resistance of the martensitic grades turns out to be limited. Nitrogen, nickel and molybdenum can be added to improve the toughness and corrosion resistance [7].

2.2.1.4 Duplex Stainless Steels

Duplex stainless steels have a mixed microstructure of austenite and ferrite. They can be thought of as chromium-molybdenum ferritic stainless steels with sufficient austenite stabilizers that permit to obtain both ferrite and austenite at room temperature. The duplex grades with equal amount of ferrite and austenite have high toughness and a better strength when compared to the single phases. They combine high strength, good toughness, high corrosion resistance and good resistance to chloride SCC [7].

2.2.1.5 Precipitation-Hardening Stainless Steels

The precipitation-hardening stainless steels are chromium-nickel grades that can be hardened by an aging treatment at a moderately elevated temperature. They combine the properties of martensitic and austenitic grades. The strengthening effect is achieved by adding elements such as copper and

aluminum, which form intermetallic precipitates during aging. The corrosion resistance is comparable to the austenitic stainless steels [7].

2.2.2 Sensitization of Stainless Steels

Sensitization of stainless steels is the process that leads to the precipitation of carbides or nitrides at grain boundaries**.** This phenomenon occurs in austenitic stainless steel when they are heated for some time in the sensitizing temperature range of about 425 to 870°C [5, 7]. The precipitation of carbides and nitrides at the grain boundaries causes the depletion of chromium in the areas immediately adjacent and renders the stainless steel susceptible in particular to intergranular corrosion, but also pitting, crevice corrosion, and stress corrosion cracking [7]. Regarding the 18/8 alloy, in terms of microstructure it can be seen that austenite containing less than about 0.03% carbon is stable, whereas $M_{23}C_6$ will be precipitated on cooling in austenite containing carbon in excess of 0.03%. This reaction is partially suppressed at rapid rates of cooling and at room temperature, leading to the formation of carbon supersaturated austenite. If this supersaturated austenite is reheated to elevated temperatures in the field of $\gamma + M_{23}C_6$ the precipitation of chromium carbides will take place preferentially at grain boundaries [6]. The combination of time and temperature can be sufficient for the carbides precipitation but not to rediffuse chromium back into the austenite adjacent to the carbides. The metallurgical methods used to avoid the sensitization of the austenitic stainless steel include the use of low carbon (0.03% maximum) alloys, post-weld heat treatment to rediffuse chromium back into the depleted areas, and the addition of stabilizers alloying elements such as titanium and/or niobium to precipitate the carbides at higher temperatures [6-7].

Ferritic stainless steels, like the austenitic grades, can also present sensitization after certain thermal treatments. Alpha ferrite has a low solubility of carbon. If it is present in solid solution at elevated temperatures (temperatures at which austenite forms) it will precipitate as carbide on cooling [6]. In this case the common remedies used for austenitic grades, such as lowering carbon content and introducing stabilizer alloying elements, do not eliminate the problem. The best remedy is to reanneal the sensitized material at about 800°C. Indeed, carbides and nitrides typically are formed at lower temperature in the range of about 400 to 700°C, causing chromium depletion in the adjacent regions. Reheated the material at higher temperatures allows chromium to rediffuse back into the depleted zones [6]. The lower sensitization temperatures of ferritic grades compared with austenitic grades can be due to the lower solubility of carbon and nitrogen in ferrite than in austenite [6].

2.2.3 Corrosion Forms of Stainless Steels

There are several forms of corrosive attack that may be encountered by stainless steels. A serious mode of attack is localized corrosion, found in stress corrosion cracking, pitting, intergranular corrosion, corrosion fatigue, and crevice corrosion. Other forms of attack that affect the stainless steels are general corrosion and attack by high temperatures gases [6]. Some of these will be briefly discussed in this section.

2.2.3.1 Pitting

Pitting is a form of localized attack that can produce penetration of a stainless steel. Typically, the initiation of pits is associated with a local discontinuity of the passive film. It can be due to a mechanical imperfection, such as an inclusion or surface damage, or a local chemical breakdown of

the film [7]. The presence of deposits on the surface and also the temperature can influence the pit initiation. In a surface not containing physical defects (inclusions, compositional heterogeneities, etc.) the initiation of pits is considered to be a result of interactions between discrete species in the environment and the passive film. Chloride is the most common agent for initiation of pitting [6]. Once the pits are formed they may continue to grow and become crevices [7].

The resistance to pitting initiation is mainly controlled by the chromium and molybdenum content in the steel. Indeed, both these alloying elements improved the stability of the passive layer and reduced the formation rate of pits. Also silicon provides a beneficial effect [5]. The content of the minor alloying elements must be controlled to avoid the formation of particular inclusions (for examples, sulfides) that can act as pitting sites [7].

2.2.3.2 Crevice Corrosion

Crevice corrosion can be seen as a severe form of pitting. It can occur within crevice or at shielded surface, where there is a stagnant solution. This form of corrosion is generally considered as form of localized corrosion, since it can destroy the integrity of mechanical joints in engineering structures [6]. Crevice corrosion is difficult to prevent. Alloys containing high-chromium and molybdenum have a better resistance against this type of corrosion [7].

2.2.3.3 Intergranular Corrosion

Intergranular corrosion is a kind of preferential attack that occurs at the grain boundaries of a stainless steel similar to the case of the sensitization. Indeed, the grain boundaries are favored sites for the segregation of solute elements or the precipitation of metal compounds such as carbides and nitrides [6]. This condition leads to the formation of regions with lower chromium content near to the grain boundary. These low-chromium zones, which may be less than one micron thick, are much more susceptible to corrosion than the remaining of the grain [5]. The intergranular corrosion can be reduced by several methods, such as [5]: solution annealing followed by rapid cooling, reducing carbon and nitrogen content in the alloy, adding alloying elements that can form stable carbides and stable nitrides. All these methods lead to the stabilization of the stainless steel and increase the resistance against the intergranular corrosion.

2.2.3.4 Stress Corrosion Cracking

Stress corrosion cracking is a particular corrosion mechanism in which the combination of a tensile stress and a corrosive environment lead to the propagation of transgranular cracks [5]. The stress corrosion cracking can bring about brittle fracture in highly ductile materials [6]. Stainless steels suffer from the stress corrosion cracking in chloride environments. The increase of temperature and the presence of oxygen tend to aggravate this form of corrosion. Furthermore, residual stresses due to production, welding or thermal cycling are often responsible for stress corrosion cracking. Even the heat treatments are not enough to completely remove these residual stresses [7]. Most ferritic and duplex stainless steels are typically more resistant to stress corrosion cracking than austenitic grades.

2.2.3.5 Corrosion by Hot Gases

Stainless steels can react with most high temperature gases to form surface scales. The rate at which the gas/metal reaction can take place through the scale is the parameter that allows us to understand if the material is useful for the given application. Obviously the desirable conditions are those which lead to a slow scale growth. A rapid scale growth is undesirable since it will quickly consume the stainless steel and causes mechanical failure when the critical dimensions are reached [6]. The most important gas/metal reactions are oxidation, sulphidation, carburization, nitriding, and attack by halogen gases [6].

Oxidation is the most common form for high temperature corrosion of stainless steels. It can occur in oxygen, air, carbon dioxide, or in more complex atmospheres containing these gases. Oxidation causes the growth of an oxide scale [8]. High temperature oxidation will be further analyzed in chapter 2.3.

Sulphidation is a kind of attack that occurs in high temperature gases containing sulfur compounds such as sulphur dioxide, hydrogen sulfide, or sulphur vapor [6]. The reaction between metals or alloys and sulphur is similar to the metal/oxygen reaction but with many metals it is much more aggressive. The reasons of the high rates for the sulphur/metal reactions are [8]: the higher diffusion rates due to the presence of defects in the structure of sulphides; the formation of low melting sulphides with the most common metals, iron, cobalt, and nickel; the low solubility of sulphur in metals, the little difference in the free energy of formation of sulphides; the high dissociation pressure of sulphides that favors the rapid intergranular corrosion of the alloy substrate. As for the oxidation resistance, the addition of chromium in the alloy improves considerably the sulphidation resistance.

Carburization and nitridation are two other kinds of high temperature corrosion. Carburization attack occurs when the alloys or metals are exposed to environments containing carbon monoxide, methane, or other hydrocarbon gases. Nitridation is found e.g. when the material is exposed to high temperature gases containing ammonia. Both carburization and nitridation can result in the formation of internal precipitates such as carbides and nitrides, causing the alloy to suffer embrittlement as well as the degradation of other mechanical properties [6, 9]. Carburization may reduce ductility and toughness of the stainless steel. It can also induce cracking in the material beneath the carburized layer, due to the high local stresses produced by the volume changes with carbide formation [6]. The addition of silicon and chromium increases resistance to carburization of the alloy [5, 9]. The increase in nickel content improves further the resistance of the alloy [5]. Regarding nitridation, high nickel contents is beneficial for the alloy, while molybdenum may be detrimental under particular conditions [6]. Nickel-based alloys are more resistant to nitridation than iron-based alloys [9].

Halogen gases are particularly detrimental to the resistance at elevated temperature of the stainless steels [5]. The alloys behave differently in halogen gases than in oxygen. Indeed, when they are exposed in halogen environments there is formation of volatile corrosion products of metal halides. For examples, the dry chlorine or dry hydrogen chlorine leads to the formation of chlorides characterized by high volatility and low melting points. In this case, the addiction of chromium and nickel improves the alloy resistance to chlorination attack. Conversely, adding molybdenum and tungsten, particularly at high concentrations, are quite detrimental since the formation of oxy-chlorides with high vapor pressures [5, 9]. Aluminium addition appears beneficial to improve the chlorination resistance, in particular at high temperatures when leading to the formation of Al_2O_3 [9]. Another halogen gas is fluorine, which is more corrosive than chlorine at elevated temperatures [5].

2.3 Nitriding of the Stainless Steel

Stainless steels can be nitrided to some degree thanks to their high chromium content. The nitriding increases the surface hardness of the stainless steels, which improves wear resistance. At the same time, the conventional nitriding temperatures (500-650°C) of the gas nitriding affect the corrosion performance of the stainless steels, because of the formation of Cr-nitrides [10]. To avoid Cr-nitrides formation, traditional nitriding for stainless steels is performed at low temperatures, below 450°C, using mainly plasma nitriding [11-14]. The formation of expanded phases (austenitic, ferritic or martensitic) due to the large amount of nitrogen that can be entrapped into the lattice [15-18] has been observed. Most studies regarding the nitriding of stainless steels have been carried out with austenitic stainless steels. Only a few have focused on ferritic and martensitic stainless steels.

Liang et al. [19] studied the surface modification of AISI 304 stainless steel by plasma nitriding. For nitriding temperatures between 430-450°C for 24 h, the nitrided layer without precipitation of nitrides was about 7-12 μm, while it was only 2-3 μm after nitriding at 350°C for 4h. Precipitates of Cr-nitrides were observed after nitriding at 465°C for 24 h. The XRD spectra showed the formation of expanded austenite at all the temperatures, with the highest saturation of nitrogen reached at 420°C. At 460°C, Cr-nitrides started to precipitate in the expanded austenite layer, whereas at 500°C some iron nitrides appeared in the nitrided layer. At this temperature, CrN, Fe_4N and Fe_3N phases were found in the nitrided layer. The formation of expanded austenite improved the wet corrosion resistance of AISI 304 stainless steel, which was instead deteriorated by the precipitation of Cr-nitrides at treated temperatures above 460°C.

Semandi et al. [20] investigated the microstructure and corrosion behavior of AISI 316 stainless steel by plasma immersion ion implantation treatment at temperatures between 150 and 520°C. The results showed that for nitriding temperatures between 250 and 450°C, both the wet corrosion and wear resistance were improved by the formation of a nitrogen-expanded austenite. At 520 °C, the extensive Cr-nitrides precipitation was accompanied by the transformation of the highly expanded austenite to martensite. This improved wear resistance of the material but deteriorated the wet corrosion resistance. The biggest depth of nitrogen penetration, about 14 μm, was obtained after nitriding at 520°C for 40 minutes. Also *Gil et al.* [21] studied the wet corrosion performance of the AISI 316L stainless steel after nitriding at 410°C for 8h. The XRD patterns showed formation of expanded austenite and precipitation of CrN. The formation of CrN in the compound layer depletes the adjacent matrix in chromium and lead to the sensitization of the material when the chromium content decreases below 11-12%.

Gontijo et al. [16] studied the S phases formed on plasma nitrided AISI 304L and AISI 316L austenitic stainless steels, and AISI 409L ferritic stainless steel. The alloys were plasma nitrided between 350 and 500°C. The presence of similar S phases layers were observed in both the austenitic (BCC) and ferritic (FCC) stainless steels. The 409L series showed the formation of a layer with high amount of nitrogen, designed in the study as expanded ferrite or ferritic S^{α}-phase. The strain state was higher for the expanded ferritic phase in comparison with the expanded austenitic phases.

Sung et al. [17] studied the phase changes of the AISI 430 ferritic stainless steel after high-temperature gas nitriding. The gas nitriding was performed at 1050 and 1100°C. The relatively high chromium content of the ferritic 430 stainless steel, enables the nitrogen to permeate into the interior. This effect is due to the strong affinity between nitrogen and chromium. The surface layer was changed into martensite plus ferrite and Cr_2N at 1050°C, while martensite plus a rectangular type retained austenite appeared at 1100°C by high-temperature gas nitriding. The high-temperature gas nitriding improved the wet corrosion resistance, while the precipitation of Cr_2N at the outmost surface area deteriorated the corrosion resistance.

Corengia et al. [22] investigated the microstructure and corrosion behavior of DC-pulsed plasma nitrided AISI 410 martensitic stainless steel. The DC-pulsed plasma nitriding was carried out at 350 and 500°C. At the lower nitriding temperatures, α-Fe and small amount of γ'-Fe_4N are detected on the surface. CrN nitrides were not detected, since the CrN precipitation takes place at higher temperature. The shift and broadening of α-Fe peaks observed on the XRD patterns, were associated with the formation of a nitrogen oversaturated phase, called expanded martensite. The presence of this expanded phases, in addition to the small Fe_4N nitrides precipitates, produces the high surface hardness observed. At higher DC-pulsed plasma nitriding temperatures, the nitrogen solid solution decomposed into α and CrN. The precipitation of CrN depletes chromium of the expanded phase and deteriorates the corrosion resistance of the alloy. The plasma nitrided AISI 410 was also investigated by Li *et al*. [23]. After plasma nitriding at 450°C for 20 hours, the surface consisted of mainly γ'-Fe_4N and ε-$Fe_{2-3}N$ iron nitrides. CrN precipitation was observed on the XRD spectrum. The formation of expanded martensite, nitrogen solid solution into the surface, was suggested also in this study. However, it could not be confirmed since the outmost nitrided layer was too thick to allow the penetration of the X-ray through to the substrate. The cross-section microstructure of the plasma treated 410 showed the formation of two distinct layers. The outer layer was considered to be a "nitrided" case rich in nitrogen, and the inner one a "carburized" layer rich in carbon.

2.4 High Temperature Oxidation

Oxidation is the most important high temperature corrosion reaction. Oxidation of metals or alloys takes place when they are heated in an oxidizing atmosphere such as air or oxygen [24]. The simplest oxidation reaction occurs when the metal interacts with oxygen to form an oxide. At the beginning the oxygen molecules from the atmosphere are absorbed on the metal surface. Here starts the nucleation of the oxides, followed by the formation of a thin oxide layer that then grows and increases in thickness. Processes like nodule formation and scale spallation may take place during the growth process of the oxide [24]. The oxide formation is regulated by the thermodynamic and the kinetics.

Thermodynamically, there will be the formation of an oxide on the surface of the metal when the oxygen potential pressure in the environment is greater than the oxygen partial pressure in equilibrium with the oxide [24]. The equilibrium pressure is determined from the standard free energy of the oxide formation. The standard free energies of formation of selected oxides as a function of temperature are plotted in diagrams known as Ellingham/Richardson. The oxidation reaction between metal (M) and oxygen gas (O_2), and the standard free energy of the oxidation reaction can be written as [24]:

$$M(s) + O_2(g) = MO_2(s)$$

$$\Delta G^\circ = -RT\, ln\left(\frac{a_{MO_2}}{a_M p_{(O_2)}}\right)$$

The thermodynamics of the reaction allows us to determine whether under conditions of temperature and partial pressure of oxygen, oxide formation is possible or not. The kinetic of oxidation reaction is also an important parameter for understanding the oxide formation and growth. Sometimes the kinetic of the process is so slow that even if there is the possibility to form the oxide,

it will take very long time to form. Furthermore, when there is the possibility to have different oxide formation, the kinetics of formation of all the oxides have to be taken into account. The rates of formation of the oxides depend of temperature, oxygen pressure, surface preparation and pre-treatment of the metal. The oxidation rate can be described using three different rate laws: logarithmic, parabolic or linear [24].

2.4.1 Oxidation of Pure Iron

Over the years, the high temperature oxidation behavior of pure iron in air or oxygen has been widely studied. The oxidation of pure iron leads to the formation of a multilayer scale, which is a mixture of three oxides: wüstite FeO; magnetite Fe_3O_4; and hematite Fe_2O_3. The composition of the scale varies with the oxygen partial pressure and the temperature [24]. The oxidation reaction is rapid at the beginning and then, under isothermal oxidation conditions, is quite steady and usually follows the parabolic rate law [8]. Moreover, oxide microstructure and oxidation kinetics strongly depend on the temperature and the sample preparation, cold working or annealing [8]. Wüstite is the less protective iron oxide and it does not form below 570°C. In this condition the oxide scale consists only of magnetite and hematite. Basically has been proposed a scale consisting of an inner magnetite layer which is thicker than the outer hematite layer [25]. Instead, above 570°C there is also the formation of wüstite and the scale appears as a multilayer of all the three oxides with wüstite close to the metal and hematite adjacent to the atmosphere [24]. Wüstite is the metal richest phase and requires the lowest oxygen partial pressure while hematite is the oxygen richest phase and requires a higher partial pressure of oxygen [24].

2.4.2 Oxidation of Carbon Steels and Low Alloy Ferritic Steels

Carbon steels are probably the most widely used engineering metal. They are extensively used for high temperature applications in power plants, chemical, and petrochemical industries. The oxidation behavior of mild steels is similar to that of iron. Carbon-steels are not subjected to strong oxidation in air for temperatures below 250-300°C and they have controlled oxidation up to 450°C. Above this temperature, and particularly above 600°C, the oxidation of the steel increases rapidly and in some cases the rate law changes from parabolic to linear [24]. The presence of carbon lowers the oxidation rates as compared to that of pure iron. The reason could be the rejection of carbon at the scale-alloy interface, causing poor contact between the scale and the alloy. During steel oxidation, decarburization may be observed at above 700°C, particularly for the steels containing relatively high levels of carbon [8].

Regarding low alloy steels, the addition of alloying elements such as manganese, silicon, chromium and nickel leads to a lower oxidation rate. Chromium-molybdenum steels are a good solution for moderate temperature applications. Chromium forms a chromium-rich scale which protects the underlying steel from further oxidation, while the presence of molybdenum increases the creep strength of the alloys [24].

2.4.3 Oxidation of Stainless steels

The stainless steels are popular materials for high temperature service. Nevertheless, they can react with many high temperature gases forming surface scales. It is important to evaluate the rate at which the gas/metal reaction takes place through the scale, since a rapid scale formation will quickly

consume the stainless steel causing mechanical failure. The high oxidation resistance of the stainless steels is typically attributed to the formation of chromic oxide, Cr_2O_3 [6].

The chromium addition as alloying element to iron can reduce the oxidation of iron, since it decreases the stability of wüstite, which is not formed during the oxidation [24]. When chromium is added in small amount there is formation of chromium-rich oxide together with iron oxides. By increasing the chromium content, the formation of iron-chromium oxide increases and the FeO layer becomes thinner compared to Fe_3O_4, since the spinel oxide slows down the diffusion of Fe^{2+} ions. A further increase of chromium leads to the formation of a mixed spinel of type $Fe(Fe,Cr)_2O_4$, which decreases definitely the oxidation rate [24]. The stainless steels differ from the other Fe-Cr alloys since the chromium content cannot be less than 11% by weight. This value corresponds to a critical concentration after which there will be the formation of an initial outer layer of pure chromia (Cr_2O_3). Above 1000°C a constant amount of Cr_2O_3 is evaporated as CrO_3 [9].

The addiction of other alloying elements, such as nickel, aluminum and silicon, further increases the oxidation resistance of the stainless steels. Instead of improving the high temperature resistance of Fe, the main purpose of Ni addition to Fe-Cr alloy is to stabilize the fcc phase which is more stable at high temperatures than the ferritic phase [24]. Aluminum is another effective alloying element that improves the oxidation resistance of the alloy. Sufficient Al addition, leads to the formation of a selective alumina scale (Al_2O_3) on the outer surface, which protects the base alloy from further oxidation [24]. Silicon, similar to nickel and aluminum, is added to the alloy because it lowers the oxidation rate. Anyway, the silicon amount must not exceed 2-3% by weight, otherwise strong embrittlement of the alloy will be caused [24].

Stainless steels typically contain several other elements, such as manganese, molybdenum, vanadium, tantalum etc., aiming at reducing the oxidation or improving their mechanical properties. Some of them, such as manganese which is added to replace partly the more expensive nickel, have a mild detrimental effect on oxidation resistance. Molybdenum and vanadium, if presented in limited quantities, have a positive effect in stabilizing the passive film in presence of chloride and also increase the resistance of stainless steels to pitting and crevice corrosion [7]. If they are present in large amount they have a deleterious effect since low melting oxides, MoO_2 and V_2O_5 can be formed leading to a catastrophic oxidation [24]. The presence of impurity such as sulfur, phosphorus or boron within the alloy is detrimental to the scale adherence and spallation resistance [24].

2.4.3.1 The Influence of Water on the Oxidation of Stainless Steels

The detrimental effect of water vapor on the high temperature corrosion resistance of the stainless steels is well known. However, the reasons for this are less understood. Several theories have been proposed to explain the high corrosiveness of H_2O/O_2 mixtures towards the chromia-forming steels.

Some studies suggest that conductivity of iron and oxygen ions through the oxide scale is enhanced by the presence of water vapor. The gaseous water molecules can transport oxygen atoms quickly through cracks and pores in the oxide [26]. Moreover, the presence of water vapor in the environment can lead to the formation of gaseous iron hydroxides that facilitate the diffusion of iron through the scale [27]. Other studies propose the increase of the grain boundary diffusion of the iron in the chromia scale in presence of O_2/H_2O mixtures [28]. It was also noted that if the H_2O content in the exposure atmosphere increases, more chromium is needed to form a protective chromia scale [29]. *Hultquist et al.* [30] observed the presence of hydrogen defects inside the chromia scale formed on pure chromium at 900°C. These defects lead to an increase of the metal diffusivity through the oxide and affect the adherence of the oxide formed.

Other investigations suggested the formation at high temperature (>1000°C) of volatile species such as CrO_3 and $CrO_2(OH)_2$. CrO_3 is formed when the Cr_2O_3 oxide layer is heated at above 1000°C in

presence of O_2. This behavior was attributed to the loss of chromium from the oxide by Cr_2O_3 evaporation, according to reaction [31]:

$$\frac{1}{2}Cr_2O_3(s) + \frac{3}{4}O_2(g) \leftrightarrow CrO_3(g)$$

Recent studies regarding the oxidation of chromia-forming alloy in water vapor/oxygen mixtures showed that chromium is vaporized also at 600°C and forms volatile chromium (VI) oxide hydroxide, probably $CrO_2(OH)_2$ [32-36].

Asteman et al. [32-33] studied the oxidation of austenitic stainless steel 304L at 600°C in presence of O_2/H_2O mixtures (10, 20, 30, 40 vol% H_2O). They detected a mass loss after prolonged exposure, which is explained by the evaporation of chromium from the surface. The Cr_2O_3 oxide formed on the alloy surface after oxidation in dry O_2 changes into a spinel-type oxide in the presence of water vapor. The outer part of the oxide and the metal adjacent to the oxide become poor in chromium. Both high water vapor content and high flow rates deteriorate the oxidation resistance of the austenitic 304L. The oxides formed close to the grain boundary are more protective compared to those formed in the center of the austenitic grains, due to the enhanced supply of Cr caused by the higher diffusivity there.

Asteman et al. further explained the oxidation behavior as a competition between the loss of chromium by vaporization and the supply of chromium to the oxide by diffusion in the alloy [34-35]. High chromium concentration, fast chromium diffusivity in the bulk (ferrite rather than austenite) and also high density of grain boundaries (small grain size) were attributed to enhance the corrosion resistance at high temperature. However, high water vapor concentration, high gas velocity and high temperature are factors that lead to a rapid corrosion of the material. For example, both the austenitic 310 and ferritic/martensitic X20 showed a controlled oxidation in O_2 + 40% H_2O at 600°C using low gas velocities. In this case the chromium-rich oxide is still protective, since the supply of chromium from the substrate of the material is quick enough to replace the chromium lost by vaporization. By increasing the gas velocities in O_2 + 40% H_2O environment the chromium vaporization becomes faster. The austenitic 310 still maintains a protective oxide layer whereas the X20 reaches the breakdown of the protective oxide all over the surface. The corundum-type oxide rich in chromium is replaced by a $Fe_{3-X}Cr_XO_4$ spinel oxide covered by hematite (Fe_2O_3) without chromium. Regarding the austenitic 304L at 600°C, was observed at both low and high gas velocities an intermediate corrosion behavior between the previous two. In this case, failure of the protective scale takes place locally, forming characteristic oxide islands. This is due to the varied chromium supply to the oxide. The oxide islands form typically on top of the alloy grain centers, since the chromium diffusion rate is slow compared to that at the grain boundaries. The upper part of the island consists also in this case of iron-rich oxide while the lower one consists of $Fe_{3-X-y}Cr_XNi_yO_4$. Austenitic 310 also show same oxidation behavior at higher O_2 + 40% H_2O gas velocities.

Segerdahl et al. [36] investigated the influence of water vapor on the oxidation at 600°C of X20 11Cr1MoV ferritic/martensitic stainless steel. The studies confirm the formation of $CrO_2(OH)_2(g)$ that depletes chromium in oxide, leading to the formation of iron-rich scale (hematite) and consequently poor protection against further oxidation. The depletion of chromium increases with the water vapor concentration and leads to breakaway corrosion after 336 hours in O_2 + 40% H_2O. The corrosion rate is 30 times greater than in dry O_2. In presence of O_2 + 10%H_2O the increase of the corrosion rate is limited if compared to that in dry O_2.

Brady et al. [37] compared the oxidation behavior between a model Fe-20Cr steel and a commercial type 430 ferritic stainless steel. These two steels were exposed at 700 and 800°C in dry air and humid air (10% H_2O), respectively of the lower chromium content, type 430 stainless steel showed a better

protective oxidation behavior in short term exposures at 700°C and up to 1000 h at 800°C in humid air, compared to the model Fe-20Cr. The greater resistance of the commercial 430 steel was explained by both considering the finer alloy grain size, which facilitates the chromium diffusion towards the oxide, and the presence of silicon, which forms SiO_2 at the alloy-oxide interface. Other differences noted were the morphology of the scales formed at 800°C in dry air. Fe-20Cr forms continuous Cr_2O_3 scales with extensive voids at the alloy-oxide interface. 430 stainless steel forms instead duplex scales, an outer $(Cr,Mn)_3O_4$ spinel layer and an inner Cr_2O_3. SiO_2 was found at the alloy-oxide interface. Only few voids were observed at the interface. The higher chromium depletion observed for Fe-20Cr than for 430 at the alloy-oxide interface suggests that Fe-20Cr has a higher susceptibility for a transition to rapid non-protective Fe-rich oxide growth in the presence of water vapor. This behavior indicates that both the finer alloy grain size and the presence of Si in the commercial 430 increase the oxidation resistance of the alloy in humid air.

2.4.3.2 Oxide Scale Formation in Presence of Water Vapor

As proposed by *Zurek et al.* [38], the oxide scale formation on ferritic steels containing roughly 10% chromium in presence of Ar-H_2O mixtures can be schematically illustrated as in **Figure 2**. The figures illustrate the oxide transformation from protective to poorly protective as a function of time.

After about 10-15 min of exposure (t_1) the alloy surface is covered by a thin protective oxide layer consisting of $(Fe, Cr)_2O_3$ and $(Fe, Cr)_3O_4$ spinel. The oxidation rate in this initial step is low since the oxide scale protects the underlying material by further oxidation. The presence of water vapor leads to the formation of volatile chromium species, such as $CrO_2(OH)_2$, and depletes the oxide scale in chromium [34-36].

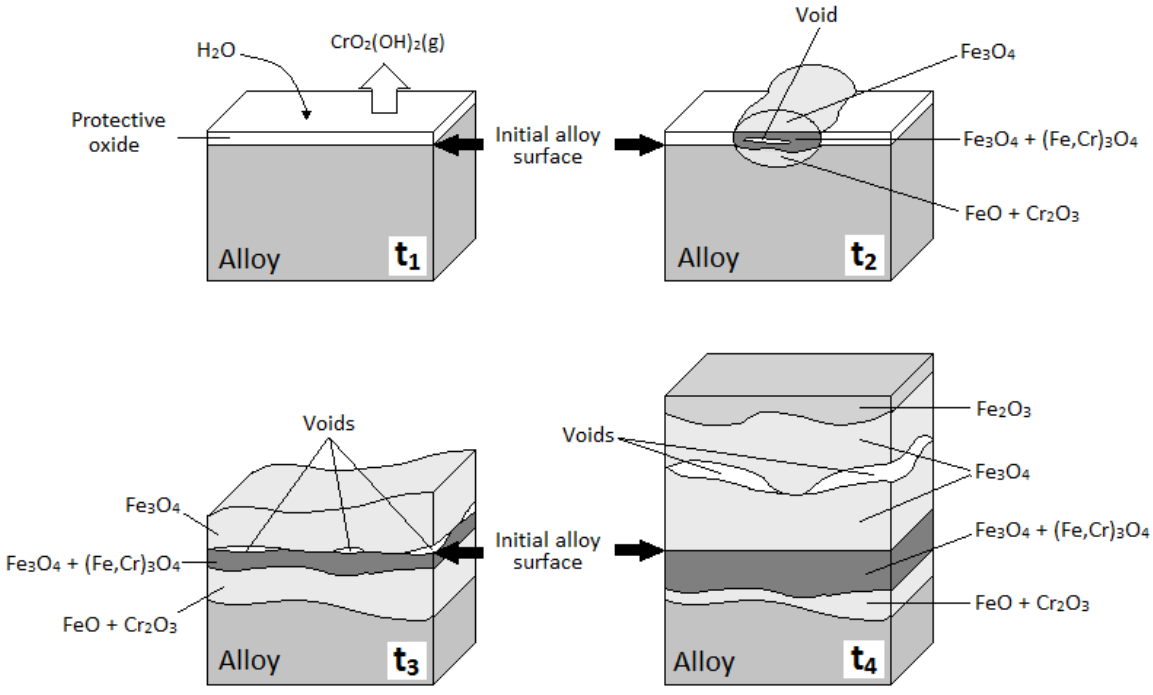

Figure 2. Oxide scale formation on ferritic 10% Cr steel exposed at 650°C in Ar-H_2O. The oxidation process is represented after subsequent exposure times ($t_1<t_2<t_3<t_4$), where t_1 is approximately 10-15 min and t_4 approximately 5h.

The Cr/Fe-ratio of the oxide scale decreases with exposure time (t_2) and the protective layer breaks down locally, causing a strongly increase of the oxide growth. Iron-oxide (Fe_3O_4) grows externally thanks to the rapid outward iron cations transport. Hematite is not formed in these initial steps since the oxygen partial pressure is lower at the oxide surface than in the gas (oxide surface is not in equilibrium with the gas). The inward transport of vacancies due to the outward iron diffusion causes formation of large voids near the initial alloy surface. Wüstite and chromia form in the inner oxide layer and the initial protective scale gradually disappears.

After further oxidation (t_3), the oxide scale grows in thickness and covers the entire alloy surface. The inner wüstite starts to change into magnetite, whereas the chromia starts to transform into $(Fe, Cr)_3O_4$ spinel oxide. Also the voids become larger because of the continuing inward transport of vacancies.

The continuous-diffusion paths between gas/oxide and oxide/alloy decrease with increasing of the void dimensions. In these conditions, the growth of the external oxide scale continues at the interface between outer and inner oxide layer. The size of the voids increases with longer exposure times (t_4) and their position tends to move outward within the outer iron-oxide scale. The diffusion of iron cations from the alloy to the scale/gas interface is hindered by both larger thickness of the oxide scale and larger size of the voids. The decrease of iron activity at the interface between oxide scale and gas results in external-hematite formation. Wüstite and chromia, within the inner oxide layer, change nearly completely into magnetite and $(Fe, Cr)_3O_4$ spinel oxide after longer exposure times.

Chapter 3

Experimental

The first part of this chapter presents a brief introduction concerning the 444 ferritic stainless steel analyzed in this work. Chemical composition, major characteristics and properties of this alloy will be given. The second part of the chapter describes samples preparation and exposure procedure used. The last part of the chapter discusses the methods used for characterization and evaluation of the corrosion behavior at high temperature for both as-received and nitrided 444 ferritic stainless steels.

3.1 444 Ferritic Stainless Steel

AISI 444 ferritic stainless steel is a low-carbon and low-nitrogen alloy with 18% chromium and molybdenum. The chemical composition is listed in **Table 1**. According to the manufacturer [39], the corrosion resistance of the 444 is good, thanks to its chromium and molybdenum contents. The pitting corrosion resistance is superior to those of austenitic grades such as 304L, 316L and 316Ti. The alloy is characterized by a good salt corrosion resistance thanks to the molybdenum content, which also increases the oxidation resistance. The intergranular corrosion resistance is high thanks to the presence of titanium and niobium that lead to an effective stabilization of carbon and nitrogen. The high chromium content and the presence of molybdenum can lead to the formation of Laves phase when the alloy is heated in the range 600 to 900°C. These phases can increase the intergranular corrosion resistance in highly oxidizing environment. Thanks to its molybdenum content, 444 shows a good resistance to the initiation of crevice corrosion, comparable to that of the austenitic 316L. Like the other ferritic stainless steels, also the 444 is insensitive to stress corrosion.

The selection of this ferritic stainless steel for application in exhaust after-treatment systems is linked both to economic aspects and to its corrosion resistance. First of all, the absence of the expensive nickel allows a reduction of the production costs if compared with the austenitic grades. The relatively high chromium level provides a good corrosion resistance and maintains also a suitable machinability and weldability of the steel. Molybdenum is generally added to 444 as a solid solution strengthener and improves the high temperature creep and the salt corrosion resistance [40]. All these properties make the AISI 444 an interesting material for application in exhaust after-treatment systems.

	Fe	C	Si	Mn	Cr	Mo	Ti+Nb
444	Bal.	0.015	0.50	0.3	17.7	1.85	0.45

Table 1. Chemical composition of AISI 444.

3.2 Sample Preparation

3.2.1 Plasma Nitriding

Plates of 444 ferritic stainless steel with a size of 65x65x1.5 mm^3 were ground and polished down to 3 µm diamond paste. The plasma nitriding was then performed by Bodycote Värmebehandling AB at about 400°C for 24h in a nitriding atmosphere with 6 vol% N_2 content in gas. The surface concentration of nitrogen was quantified by using XPS analysis and the thickness of the nitrided layer was estimated by SEM/EDS cross-section analysis.

3.2.2 Sample Preparation Before the Exposures

The as-received 444 ferritic stainless steel with a thickness of 1.5 mm was first cut to coupons with a size of 15x15 mm^2. Before oxidation test, one side of each specimen was mechanically ground on SiC-paper to 1200 mesh, polished with 6 and 3 µm diamond pastes, and then cleaned in isopropanol by using ultrasonic agitation.

Regarding the nitride samples, coupons of about 15x15 mm^2 were cut from the plate of the test material. Before oxidation test, re-polishing was done by using 3 µm diamond paste for another 7 minutes, aiming removing any possible reaction layer and obtaining a more homogenous concentration of nitrogen. The aim is to understand the role of nitrogen uptake in exhaust systems and no reaction layer has been observed there. All the samples were cleaned in isopropanol by using ultrasonic agitation before the exposures.

3.2.3 Choice of Nitrided Samples for the Exposures

Coupons were cut from the nitrided plate of AISI 444. The plasma nitriding (DCPN) produces a glow-discharge on the component surface, which can cause electrical problems such as the edge effect, hollow cathodic discharge, and arcing. This results in non-uniform thickness of the nitrided surface layer [11]. Several areas with different shades are in fact visible on the nitrided plate. The most homogeneous region, in terms of nitrided layer, seems to be the center of the plate. Our samples exposed for 24 hours were cut from this area. The other samples were cut from the surrounding area which was supposed to have a slightly varied nitriding layer thickness.

3.2.4 Sample Preparation for the SEM/EDS Cross-Section Analyses

SEM/EDS cross-section analyses were performed on the nitrided samples before and after oxidation for 24 and 168 hours. A slice of metal was first cut from each sample by using a diamond blade. The surfaces of interest were then covered with a thin nickel layer by using physical vapor deposition. Subsequently, they were mounted in PolyFast resin. Nickel coating was used to avoid damage of the edges during grinding and polishing. The mounted samples were ground and polished down to 3 µm diamond paste by using a semi-automatic system.

3.3 Experimental Setup for Exposure

The laboratory exposures were carried out in a horizontal tube furnace with a 75mm diameter. **Figure 3** shows the experimental setup for having a constant humidity level by controlling the water bath temperature. The temperature of water bath was 46°C, which resulted in water volume concentration of 10%. Heating tape was rolled around the tube between the flask and furnace to avoid the water condensation. The as-received and nitrided 444 coupons were exposed in humid air at 450°C, 500°C, 550°C and 600°C for 24 and 168 hours with a constant flow rate 6000ml/min. duplicates for both as-received and nitride samples were used for each exposure using an alumina holder. The polished surface of the coupons was positioned parallel to the direction of the gas flow. After exposure, the air flow was turned off and the samples were left in turned off furnace until cooling to room temperature.

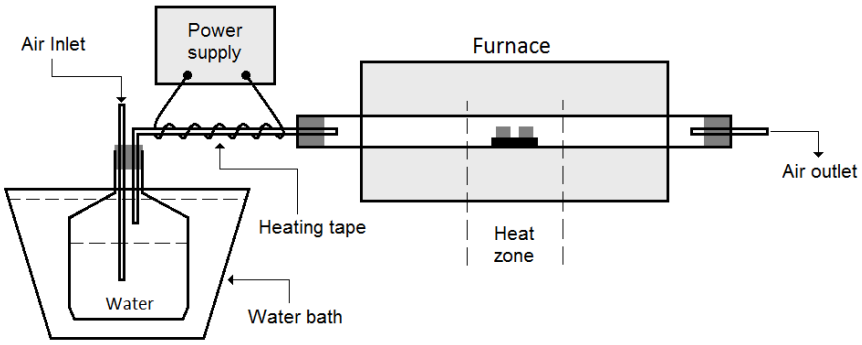

Figure 3. Experimental setup used for the oxidation in air with 10% water vapor.

3.4 Analysis Techniques

Several techniques were applied in this study in order to investigate the effect of nitridation on the oxidation behavior at elevated temperatures and the related phase and microstructure development in the AISI 444, as presented in the following part.

3.4.1 LOM – Light Optical Microscopy

Two optical microscopes used in this study were a Zeiss Discovery V20 stereomicroscope and a LEICA Leitz DMRX microscope. The optical microscopes were mainly used for preliminary inspections of the samples before and after oxidation. It was observed that the microstructure of the material was revealed by the etching effect of the plasma during nitriding. The stereomicroscope gives a good overview of the specimens and allows the identification of the most interesting regions for the subsequent analyses of the oxidized samples. Stereomicroscope was also used during the process of sample preparation to check the polishing quality on the surface of the samples before the exposures.

3.4.2 SEM – Scanning Electron Microscopy

The Scanning Electron Microscopy used was a SEM LEO 1550 with GEMINI field emission gun (FEG-SEM). The Scanning Electron Microscopy presents three main advantages compared to the optical microscopy: better resolution; large depth of focus; and atomic contrast. The SEM uses convergent electron beam instead of photons in ordinary optical microscope. The shorter wavelength of electrons allows higher resolution, theoretically up to 10 nm. When the convergent electron beam hits the sample surface, the electrons excite the sample matter within the interaction volume. The adsorbed energy can be released in different ways through the entire interaction volume. The signals include secondary and backscattered electrons, Auger electrons, X-Ray fluorescence. All the signals are detected by different detectors within the SEM and provide a variety of information about the sample. The secondary electrons (SE) mainly give information regarding the surface topography. The backscattered electrons (BSE) give additional information about the composition of the material. Heavier atoms, with more electrons have a higher probability for backscatter. The Auger electrons have a very low energy and therefore their escape depth is very short. Only the Auger electrons produced from the top atomic layers of the interaction volume are detectable but normal SEM instruments are not equipped for that. The X-rays generated by the electronic transitions in the atoms give information of the chemical composition in the analyzed area. They are measured by using EDS detector.

In this work, Scanning Electron Microscopy was mainly used to analyze the top surfaces of the as-received and nitrided samples and the cross-sections of the nitride sample, both before and after oxidation. Surface morphology for each sample was investigated by both low and high magnification using two secondary electrons detectors: InLens for improved resolution at higher magnifications, SE2 for the better topography visualization at low resolution. For the cross-section Back Scattered Electrons detector (Centaurus) was used, since it allows a better distinction of the oxide layers formed after the exposures. Sample preparation including grinding and polishing was needed prior to cross-section analysis.

3.4.3 EDS – Energy Dispersive X-ray Spectrometry

Energy Dispersive X-ray spectroscopy was performed by using an Oxford Instruments INCA PentaFETx3 system, attachment to the SEM. The EDS allows chemical analysis of the specimen. The EDS detector measures the intensity of the X-ray photons generated by the inner-shell ionization in the sample. When the electron beam hit the specimen, an electron in an inner shell can be excited and kicked out from the shell creating an electron hole. Subsequently, an electron from an outer shell with higher energy fills the vacant, and the energy difference between the two shells is released in the form of an X-ray. Each X-ray has a characteristic wavelength that corresponds to a typical electronic transition of the excited atom. By counting the number of X-rays having the same energy, it is possible to quantify the amount of the element in the volume analyzed. X-rays can also be produced by fluorescence and by decelerating of the electron beam. In the first case, an X-ray with enough energy can ionize an atom, which in turn releases a lower energy photon. This increases the intensity of the low energy peak but is detrimental to the intensity of the higher energy peak. This effect has to be taken into account for the element quantification. Finally, others X-rays can be produced by the energy released because of deceleration of electron beam in the Coulombic field of the atoms. These constitute the background of EDS spectra. Drawback of EDS is its low sensitivity for the light elements.

Regarding EDS study in this work, quantitative point analysis and qualitative line scans and mapping were employed. For as-nitrided samples, EDS was performed to estimate the thickness of the

nitriding layer. The chemical composition of the surface oxide and the cross-section of the oxide scales formed were also inspected by this method for both as-received and nitride samples after oxidation. Due to the relative large interaction volume, quantitative analyses of small precipitates and thin layers by EDS are difficult. However qualitative line scans and mapping are still useful for providing indicative information regarding elemental distribution within the alloy and the oxide scales.

3.4.4 XPS – X-Ray Photoelectron Spectroscopy

X-ray Photoelectron Spectroscopy was performed by using a PHI 5500 with an AlKα X-ray monochromator with hν = 1486.6 eV. The depth profiling was carried out by using an argon ion gun with etch rate calibrated on T_2O_5. The PHI Multipack software, with sensitivity factors by the instrument producer, was used for the data evaluation. XPS, also known as Electron Spectroscopy for Chemical Analysis (ESCA), is a surface sensitive technique, which allows both qualitative and quantitative analyses of the elemental composition of the surface analyzed. It also allows the identification of the chemical state and provides information regarding electronic structure of the elements detected. The analysis area is about 0.8 mm^2 under the current experimental setting. The principle behind XPS is related to the ejection of an electron from a core level of an atom when excited by an X-ray photon of energy hν. The spectrometer measures the kinetic energy (E_k) of the photoelectron emitted, which in turn depends on the energy of the incident X-Ray. The binding energy (E_B) of the electron is the intrinsic property of the material and can be calculated from the following equation:

$$E_k = h\nu - E_B - \varphi$$

where φ is the spectrometer's work function in a range of several eV and is characteristic of its experimental configuration. Approximately, all the electrons with binding energy lower than the energy of the X-ray photon will appear in the spectrum.

In this study, XPS was used to analyze the surface of as-nitrided samples in order to determine the composition and nitrogen concentration in the first few nm of the nitrided layer. It is also used to determine the composition and thickness (by depth profiling) of the surface oxide for both as-received and nitrided coupons after oxidation.

3.4.5 XRD – X-Ray Diffraction

X-ray Diffraction was performed by using a Bruker AXS, D8 Advance X-ray Diffraction system (Cr kα-radiation) operated at 35 kV and 40 mA. In order to have X-ray diffraction the lattice must meet the following requirements: interplanar distances comparable to the wavelength of the incident radiation, and scattering centers spatially distributed in a highly regular way. These conditions are satisfied by the crystalline lattice. The X-ray beam is diffracted by the crystalline lattice of the material at certain angles of incidence θ, according to Bragg's law:

$$n\lambda = 2d_{hkl}sin\theta$$

where n is an integer, λ is the wavelength of the incident X-ray beam and d_{hkl} is the distance between atomic layers of the set of crystalline planes. When the angle of incidence satisfies the equation, the interference is constructive and the X-rays appear to be reflected from the crystal. At all the other angles the interference is destructive.

During this work X-ray diffraction was performed on the as-nitrided material with the purpose of identifying the phases formed after plasma nitriding. XRD was also performed on the oxidized as-received and nitrided coupons to identify the phases formed after exposure. The setups used for the analyses were Bragg-Brentano (BB-XRD) and grazing incidence (GI-XRD). The grazing incidence XRD is more surface sensitive, because small angle between the incoming beam and the sample surface (3°) leads to small information depth. The GI-XRD setup was used for the characterization of as-received samples, since the oxide layer is particularly thin. BB-XRD setup was used for the nitrided samples both, before and after oxidation.

Chapter 4

Results

The following chapter is dedicated to the results obtained during this project. The samples were characterized by several analytical techniques, including Light Optical Microscopy (LOM), Scanning Electron Microscopy (SEM), Energy Dispersive X-Ray Spectrometry (EDS), X-Ray Photoelectron Spectroscopy (XPS), and X-Ray Diffraction (XRD). The results of each from these analyses will be show in separated part.

4.1 Light Optical Microscopy (LOM)

Preliminary analyses were done on all the samples before and after exposure by using optical microscope and stereomicroscope. First some top surface micrographs from plasma nitrided 444 will be reported and then surface morphology after exposure of as-nitride 444 at different temperature and time will be revealed by using stereo microscope.

4.1.1 As-Nitirded Material

The microstructure of the as-nitrided 444 without re-polishing is shown in **Figure 4a**. The structure was revealed by the etching effect of the plasma during nitriding. At higher magnifications, as seen in **Figure 4b**, parallel slip bands occur on a few of crystallographically equivalent planes and also some

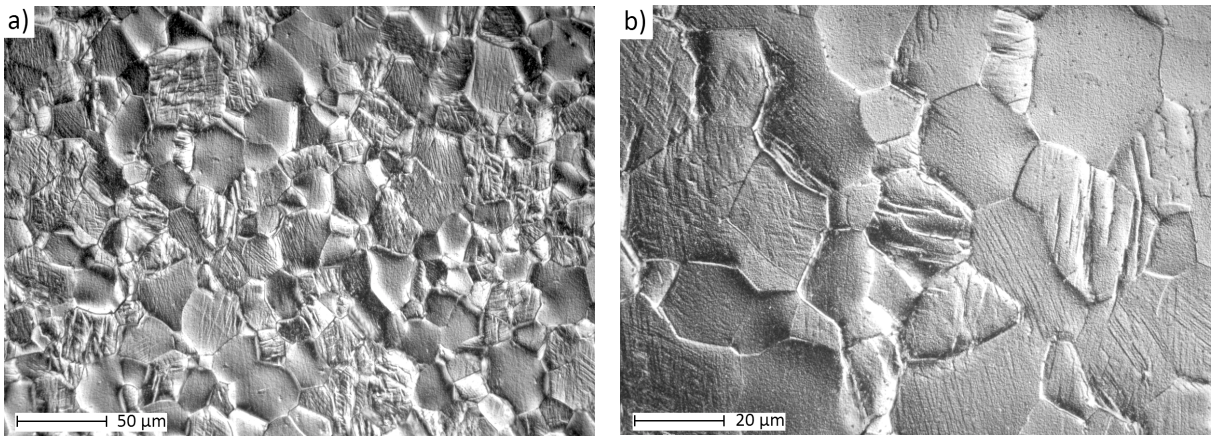

Figure 4. Optical micrographs of as-nitrided 444. a) Grain structure revealed by the etching effect of the plasma during nitriding, b) slip bands are visible inside the grains at higher magnification.

intergranular cracks are visible. This surface morphology can be an indication of the plastic deformation associated with the formation of S^{α}-phase. This S^{α}-phase is considered to be a supersaturated solution of nitrogen in the ferritic phase and precipitates in α phase. It has been reported that CrN is formed at temperature above 450°C [11]. Similar to the austenitic grades [41], in ferritic stainless steels the lattice seems to expand by interstitially dissolved N. Consequently, high stresses are induced, leadings to the formation of cracks.

4.1.2 Oxidation of Nitrided Material

Figure 5 shows stereo micrographs of four nitrided coupons after oxidation for 168 hours at different temperatures. The presented samples were taken from the edges of the initial nitrided sheet. They are second-choice specimens, since compromised by the edge effect of plasma nitriding process. These samples were used for the SEM/EDS cross-section analysis. As can be seen clearly, the oxidation of the samples is not homogenous on the entire surface. Areas with different oxidation grades are visible and can be recognized on the stereo micrographs thanks to the various shades of grey. This different oxidation could be due to gas flows within the tube furnace, sample position on the holder, microstructure differences etc. By using only micrographs is difficult to identify the more oxidized regions.

Areas with different oxidation grades are visible also on the samples obtained from the center of the nitrided sheet and exposed for 24 hours. For these samples the oxidation is generally more uniform, since the nitrided layer should be more homogeneous. The samples are not shown.

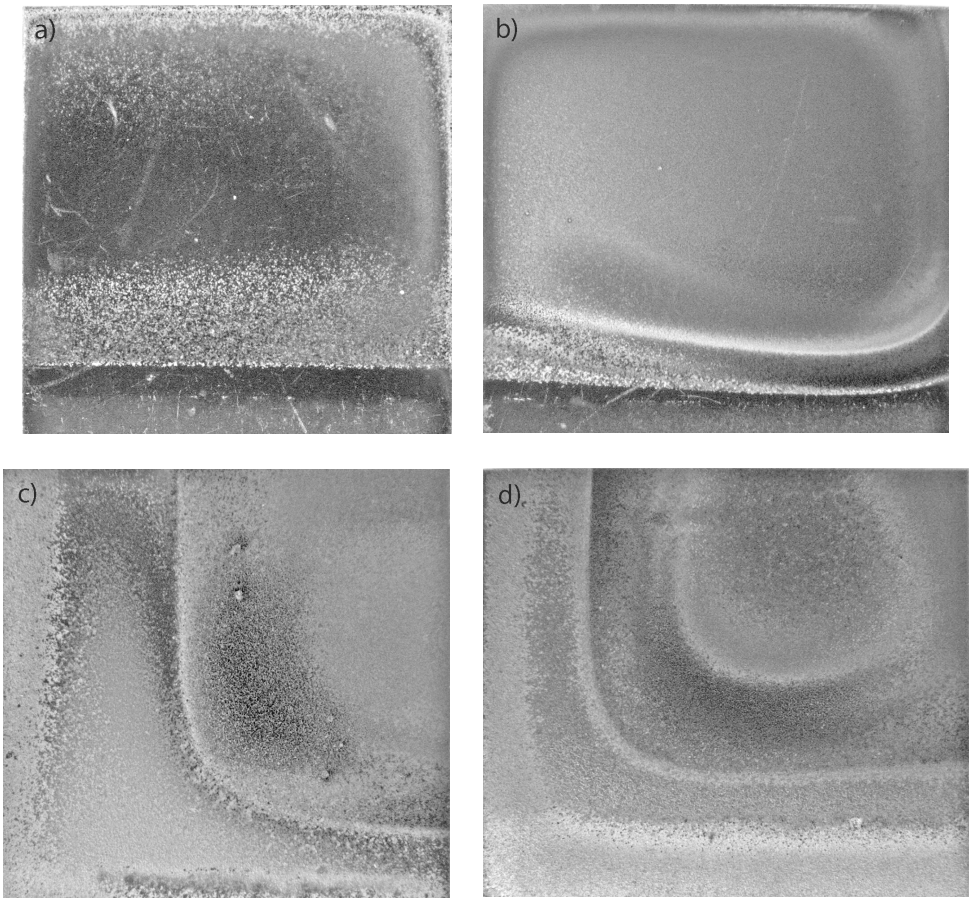

Figure 5. Stereo micrographs of nitrided 444 exposed for 168h; a: 450°C, b: 500°C, c: 550°C, and d: 600°C. The samples were used for the SEM/EDS cross-section analyses.

4.2 Scanning Electron Microscopy (SEM) – Energy Dispersive X-Ray Spectrometry (EDS)

The results obtained by using SEM are shown in this section which is further divided in two parts. The first one is dedicated to the as-nitrided material whereas the second one presents the result obtained from both the as-received and nitrided material after oxidation in 10% H_2O for 24 and 168 hours. Each part shows some images including the top view and cross section of the samples. EDS analyses were performed in order to acquire corresponding chemical information. It should be noticed that quantifications of light elements by EDS might be problematic.

4.2.1 As-Nitrided Material

Figure 6 shows the surface morphology after re-polishing of as-nitrided 444 (see sample preparation in chapter 3.2). The images were taken using back-scattered electron detector (BSE), which gives additional compositional contrast.

Figure 6a is a low magnification top view of the specimen. The grain structure of the material is clearly distinguishable thanks to the different grain orientations, associated with different grayscale. **Figure 6b** gives a higher magnification of superficial cracks, which are also visible in **Figure 6a**. Internal cracks are also visible on the cross sections of the oxidized samples in **Figure 10**-**17**. The formation of these intergranular cracks can be associated with both the plasma nitriding and the sample preparations. Plasma nitriding introduces a large amount of nitrogen to the ferritic lattice of the 444 and charges the structure with high stresses, resulting in the formation of cracks.

The thickness of the nitrided layer, determined by using SEM/EDS cross-section analyses, is about 10-20 µm. The thickness of the layer is dependent on the area where the analysis has been done.

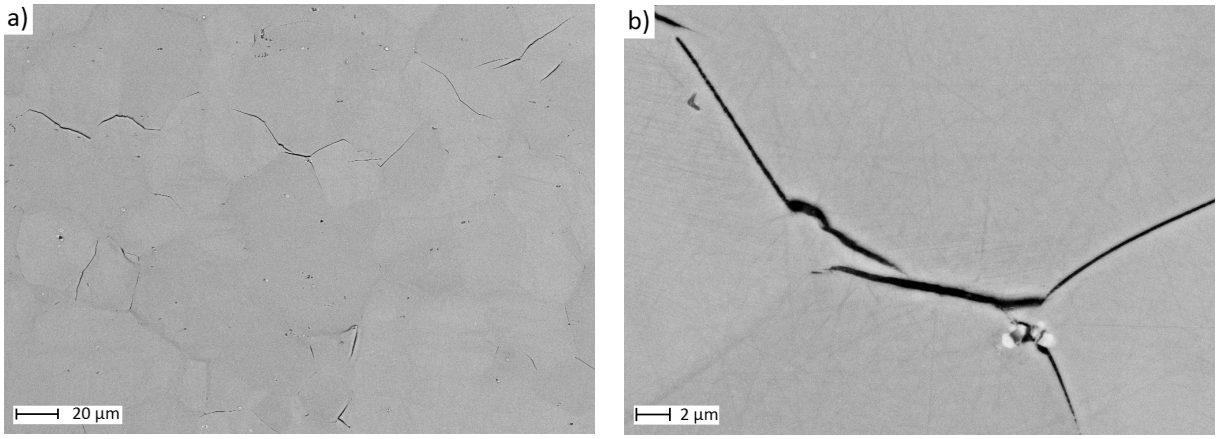

Figure 6. Surface morphology of as-nitrided 444. a) top view at lower magnification, and b) higher magnification of surface cracks.

4.2.2 SEM/EDS Top Surface Morphology

4.2.2.1 As-Received Material After Oxidation

Top views of oxidized as-received specimens are shown in **Figure 7**. Almost the same surface morphology was observed on all the oxidized as-received samples, independent of exposure temperature and exposure time. The images presented here are representative for the oxidation of the as-received 444 samples. **Figure 7a** shows the surface of as-received material oxidized at 500°C for 24h.

As can be seen from the picture the surface is still smooth and the oxidation is rather limited. Only some scattered oxide particles are observed after 24 hours of exposure. **Figure 7b** shows the surface morphology of the sample oxidized at 550°C for 168h. Also at these exposure conditions only a slight oxidation of the sample surface is detected. It seems that more scattered oxide particles are formed under these conditions. The inserts in **Figure 7** show the oxides found on the surface at higher magnifications. EDS analyses reveal the presence of both iron and titanium in the oxides. These oxides might be related to inclusions in the alloy.

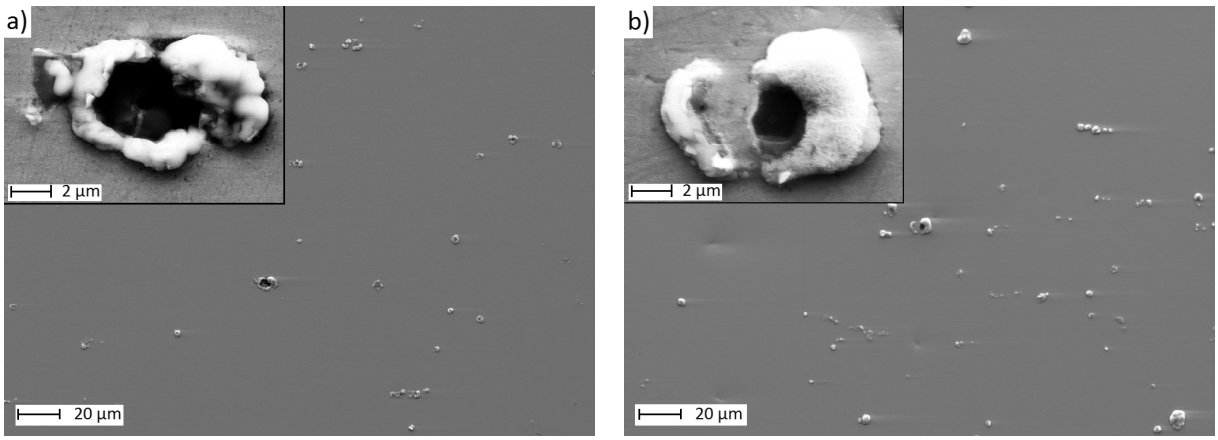

Figure 7. SEM pictures. Surface morphology of as-received 444 oxidized in 10% H_2O at a) 500°C for 24 h and b) 550°C for 168 h. The insert indicates (Fe-Ti) oxide particles at higher magnification.

4.2.2.2 Nitrided Material After Oxidation

Figure 8 shows top-view of the oxide scale formed on nitrided samples exposed for 24 hours in 10% H_2O. It is clear that the nitrided samples are more oxidized than the as-received samples exposed at the same conditions. The second observation is the preferential oxidation at the grain boundaries and on some grains with particular lattice orientations **(Figure 8c)**. Although the thickness of the oxide layers formed on the surface cannot be determined by using the SEM top views, some information regarding the oxidation extent can be deduced. By comparing the four samples, it is clear that the lowest oxidation rate is for the exposure at 600°C. The oxide formed on the nitrided material is particularly thin at this temperature.

The morphology at low magnification (**Figure 8d**) is rather similar to that observed from the as-received material after oxidation. The surface cracks and, some oxide particles are also observed. The insert in **Figure 8** with higher magnification provides more details for the oxide. It is revealed by EDS that the oxide particles formed at 450 and 500°C are Fe oxides, while oxide nodules (diameter of

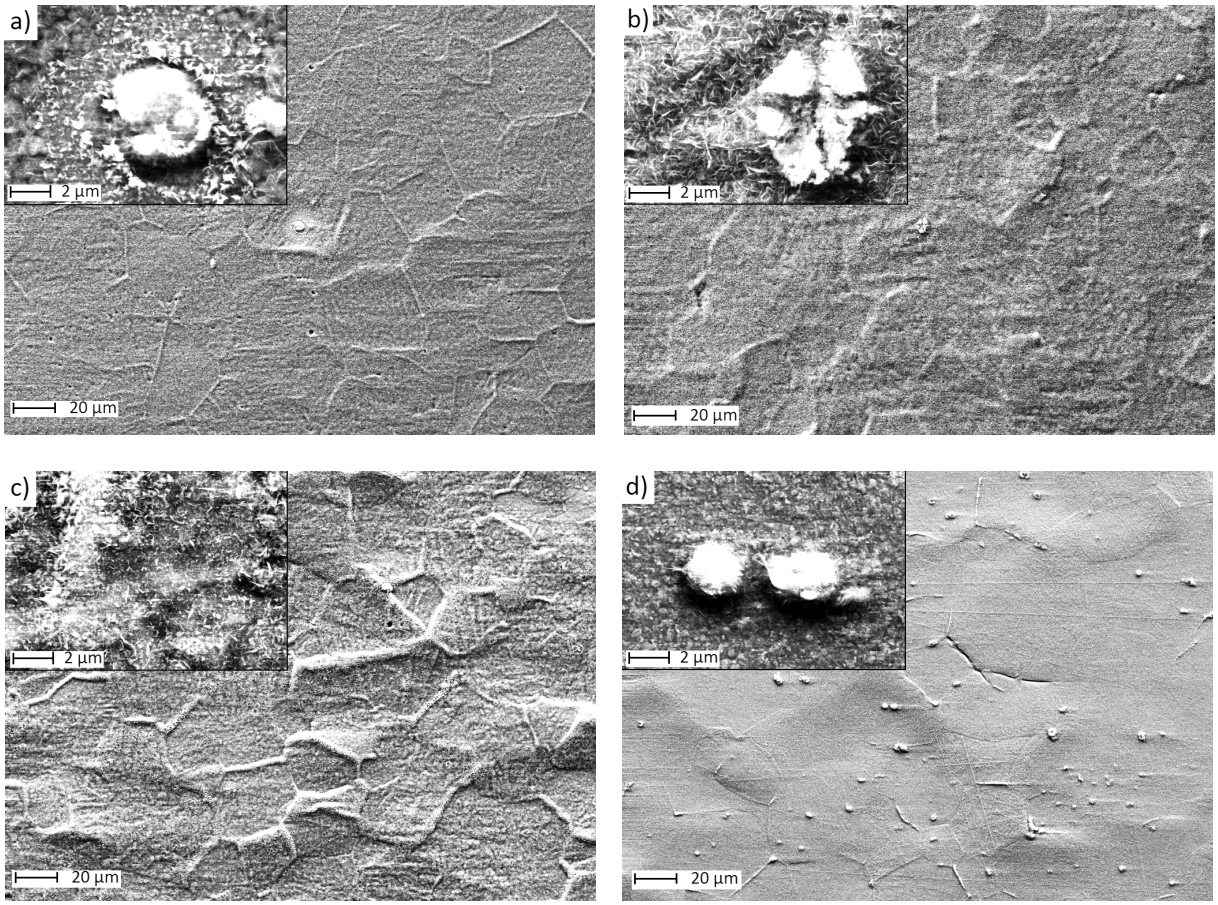

Figure 8. SEM pictures. Surface morphology of 444 oxidized 24 h in 10% H_2O with inserts at higher magnification; a: 450°C, detail of Fe oxide particles; b: 500°C, detail of Fe oxide particles; c: 550°C; d: 600°C, detail of (Fe-Ti-Nb) oxide particles.

a few microns) containing traces of titanium and niobium are formed at 600°C. Moreover, at lower temperatures the surface is covered by whiskers oxide. This oxide becomes less lengthened and sharp at 550°C. At 600°C it seems that the whiskers oxide is less developed.

Figure 9 shows top-view of the oxide scale formed on nitrided samples exposed for 168 hours in humid air containing 10% H_2O. The surfaces appear generally more oxidized compared to those with shorter exposure time. Inconsistent with observations for 24 hours, oxidation at 550°C seems to be rather limited after 168h. This might be attributed to the sample chosen. It has lower N content or the oxidation is not homogenous on the entire sample. Further investigation is needed. At 450°C more pronounced oxidation can be seen at the grain boundary and grains with special lattice orientations. The higher magnification shows the formation of a thick needle-shaped oxide layer.

Similar to the short exposure time, the most oxidized samples seems to be the one exposed at 500°C after 168 hours. The surface is completely covered by a thick oxide layer. Also at this temperature the oxidation takes place preferentially at the grain boundaries and grains with special lattice orientations. At higher magnification the needle-shape oxide layer is formed. The oxidation at higher temperatures seems to be weaker also at longer time of exposure. Both the samples exposed at 550 and 600°C show more homogenous oxidation layers. Some oxide nodules can be found on these two samples.

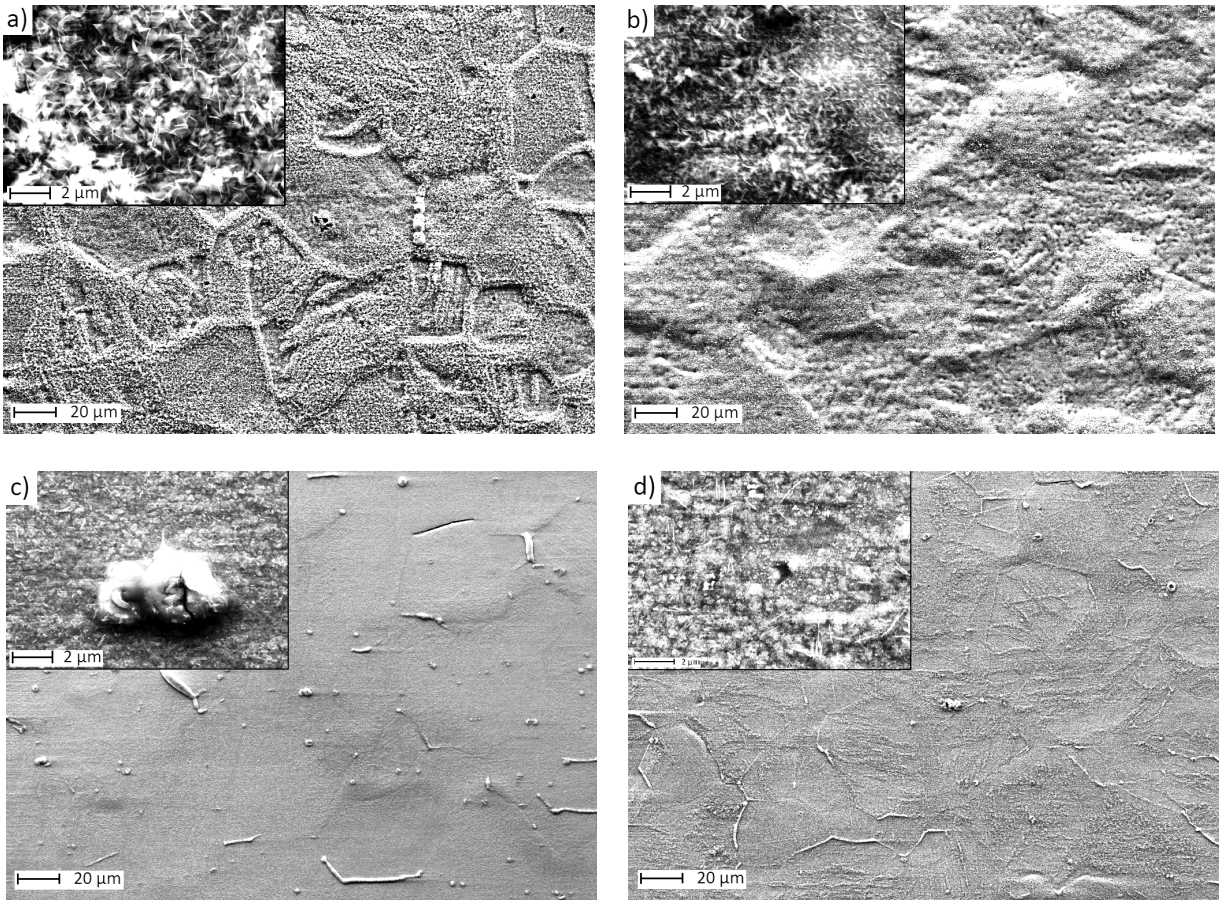

Figure 9. SEM pictures. Surface morphology of 444 oxidized for 168h in humid air containing 10% H_2O at a) 450°C; b) 500°C; c) 550°C; d) 600°C.

4.2.3 SEM/EDS Cross-Section of Nitrided Samples

Figure 10-13 show the SEM cross-sections of the samples oxidized for 24 hours in 10% H_2O. The images were taken by using Back Scattered Electrons detector, which allows a clearer identification of the oxide layer formed on the alloy.

The bright white layer, that covers the oxide, is nickel deposition used for the sample preparation. As can be seen at low magnification, the oxide scales formed after exposures for 24 hours at different temperatures appear quite homogeneous along the whole analyzed areas. Possibly slight grain boundary corrosion is observed in **Figure 11c-13c**. All the samples formed a duplex oxide scale, consisting of an outer region of iron oxide and an inner subscale of chromium-richer oxide according to elemental EDS line scans. The non-protective outer iron-rich oxide scale is consistent with the literature which reports the detrimental effects of water vapor on oxidation of stainless steels [32-36].

The thickness of the oxides changes from 0.65 µm, measured on the cross-section sample exposed at 600°C, to 1.70 µm, for the sample exposed at 500°C. The thicknesses of the oxides formed at 450 and 550°C are quite similar, 1.40 and 1.45 µm respectively. A third distinct and quite thick layer is observable below the oxide scale of the samples exposed at 450, 500 and 550°C. The elemental EDS line scan analyses detect the presence of oxygen also in this region, but the low amount does not allow formation of oxide scale. In this region, atomic oxygen dissolves into the alloy at the

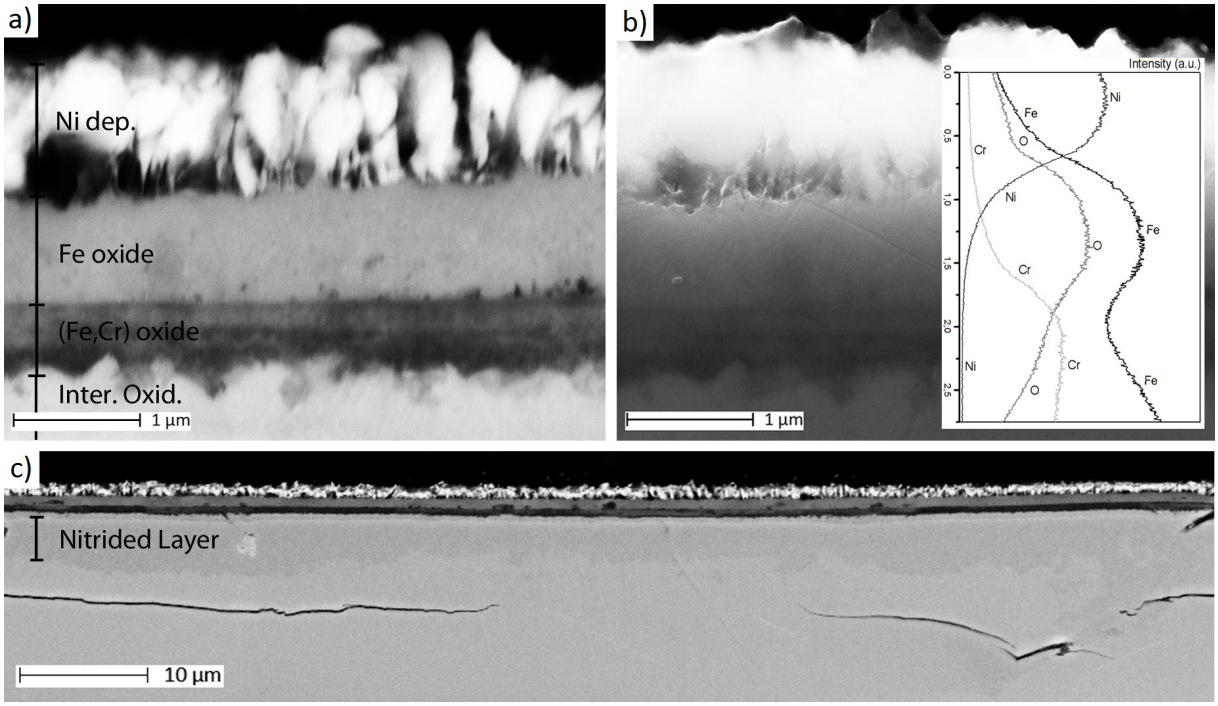

Figure 10. SEM cross-section of 444 after oxidation at 450°C, 24 h in humid air containing 10% H_2O; a) detail of the oxide layer recorded in Back Scatter mode; b) EDS line scan of the oxide layer; c) overview of the oxide layer, Back Scattered Electron image (BSE).

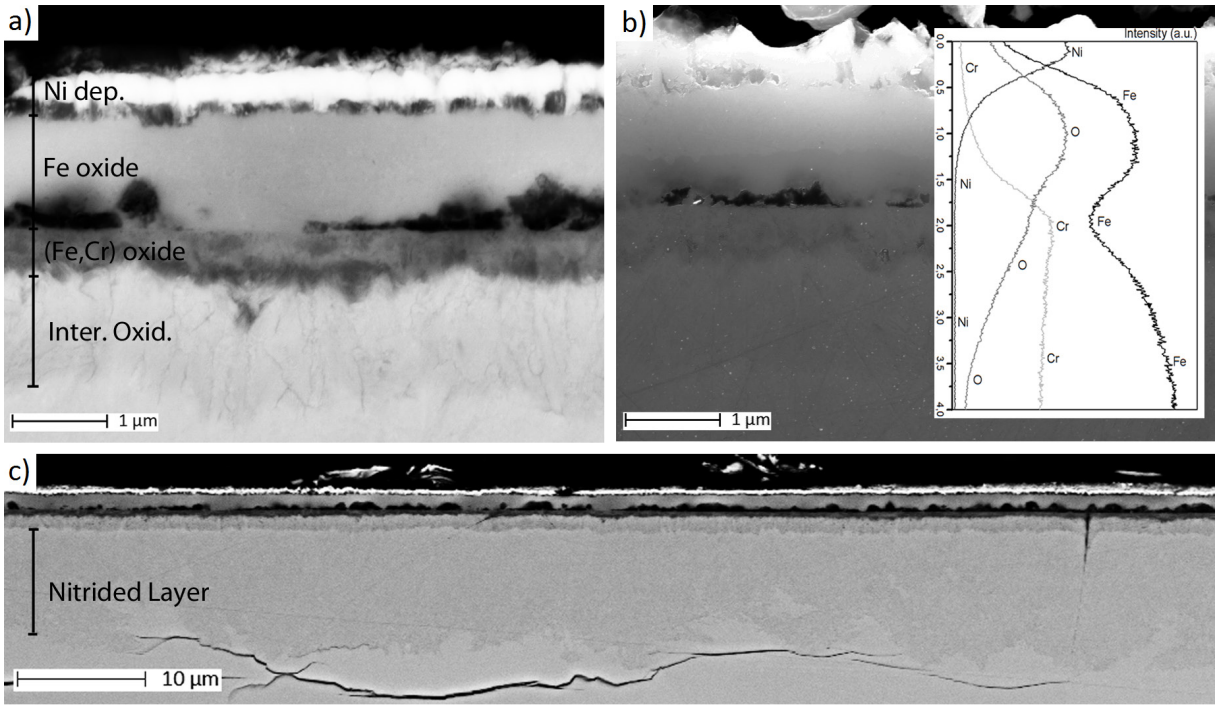

Figure 11. SEM cross-section of 444 after oxidation at 500°C, 24 h in humid air containing 10% H_2O; a) detail of the oxide layer recorded in Back Scatter mode; b) EDS line scan of the oxide layer; c) overview of the oxide layer, Back Scattered Electron image (BSE).

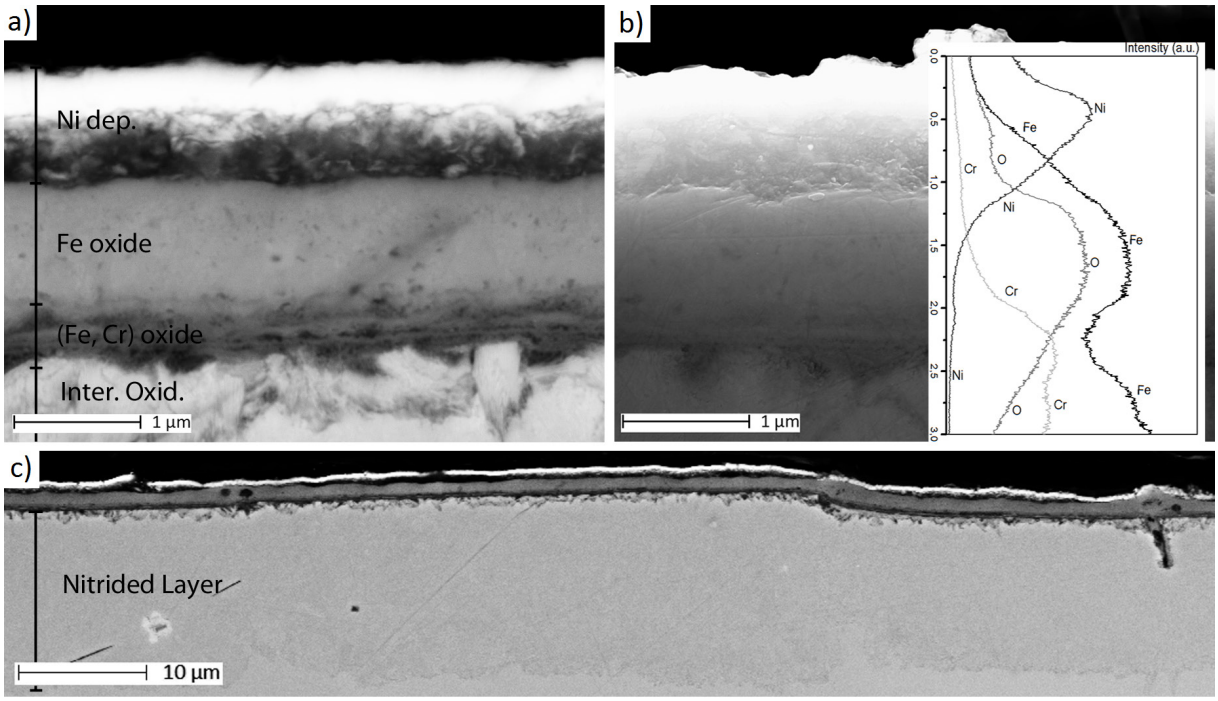

Figure 12. SEM cross-section of 444 after oxidation at 550°C, 24 h in humid air containing 10% H_2O; a) detail of the oxide layer recorded in Back Scatter mode; b) EDS line scan of the oxide layer; c) overview of the oxide layer, Back Scattered Electron image (BSE).

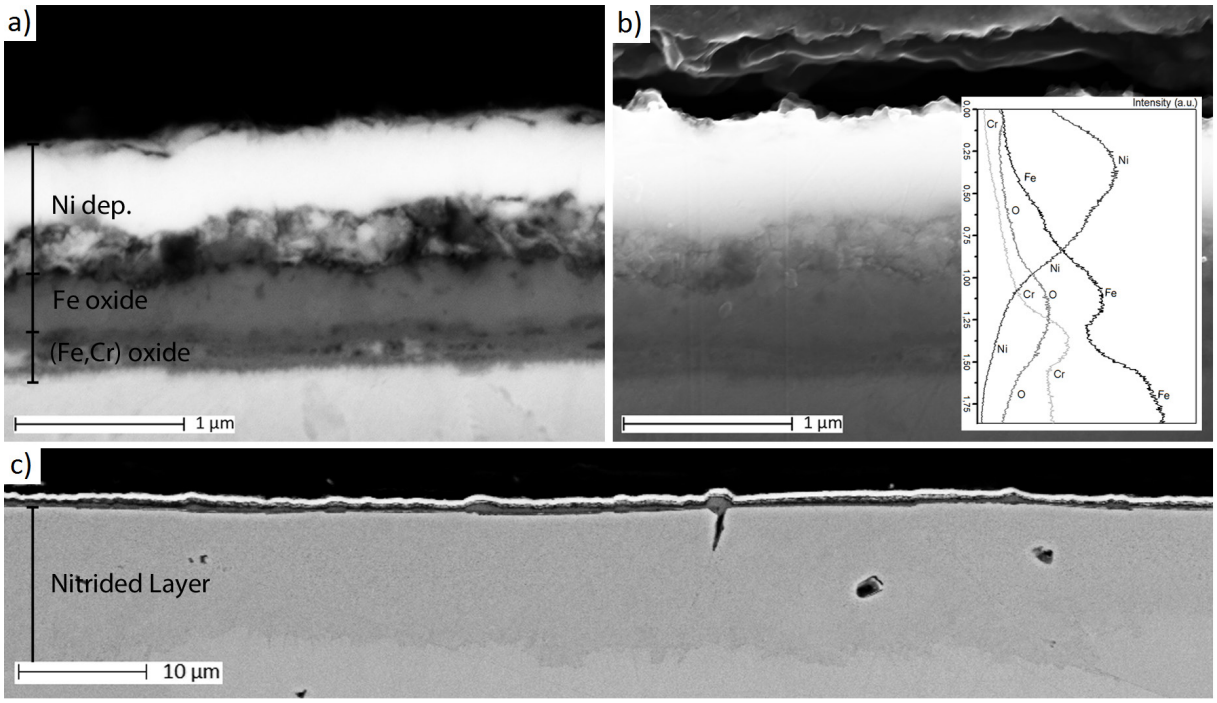

Figure 13. SEM cross-section of 444 after oxidation at 600°C, 24 h in humid air containing 10% H_2O; a) detail of the oxide layer recorded in Back Scatter mode; b) EDS line scan of the oxide layer; c) overview of the oxide layer, Back Scattered Electron image (BSE).

oxide-metal interface and diffuses into the metal matrix to oxidize the more reactive alloying elements causing internal oxidation. About the other alloying elements, the results obtained from elemental EDS line scans through the oxide scale indicate enrichment of molybdenum, nitrogen and silicon within the inner oxide layer at all temperatures. The EDS depth profiles for these elements are not shown in **Figure 10b-13b** since their low content within the alloy.

Isolated void formation is observed at the inner and outer oxide interface for the samples exposed at 450 and 500°C. The oxide formed at higher temperature seems to be more compact and adherent than the others seen at lower temperature. At 600°C, the oxide is particularly thin and compact. No void formation is observed at this temperature and also the internal oxidation seems to be absent or very reduced.

Interesting is also the nitrided layer observed on the lower magnification images for all the samples. As can be seen in **Figures 10c-13c**, the thickness of the nitrided layer is not constant along the entire analyzed sections and seems to be influenced by both the microstructures of the alloy and the surface finishing of the samples. Also the mean value of nitrided layer thickness measured for each analyzed section is different from the others and confirm the non-homogeneity of the plasma nitriding process.

Figures 14-17 show the SEM cross-sections of the samples oxidized for 168 hours in humid air containing 10% H_2O. The images were taken by using Back Scattered mode. As can be seen in low magnification images, the oxide scales formed for the longer time exposures are generally thicker than the ones from the 24 hours exposures. The oxidation is quite homogeneous along the analyzed cross-sections of all the samples, with possibly slight grain boundary corrosion, as seen in **Figures 15c and 17c.**

Even for the 168 hours exposures, the worst conditions for the oxidation are reached at 500°C. The oxide scale formed at this temperature is about 5 µm, consisting of a thick and non-protective outer iron oxide and an inner chromium-richer oxide. Also the internal oxidation is pronounced, the speckled layer is thicker than 3 µm. The thicknesses of the other oxide scales, measured on the SEM cross-sections, are 3.45 µm, 3.70 µm, and 2.70 µm, respectively for the exposure at 450, 550 and 600°C. At higher temperatures the oxidation is weaker also for the 168 hours exposure.

The elemental EDS line scans show the formation of a more protective oxide scale at 550 and 600°C. At these temperatures the inner oxide shows an increase of the chromium content, which improves the protective properties of the oxide against the further oxidation. The content of the alloying elements, such as molybdenum, nitrogen, and silicon, increases in the inner oxide layer. Also the manganese content increases within the inner oxide layer. This unusual result disagrees with as reported in literature [32, 35, 40]. This increase of manganese content within the inner oxide layer is probably due to an overlap problem with the chromium signal. The silicon distribution inside the scale is also of interest. At lower temperatures, enrichment of silicon is detected in the entire inner oxide layer, as for the other alloying elements. At 600°C the EDS line scan of the element confirms a greater concentration of silicon at the alloy-oxide interface. The EDS map of the Si, **Figure 17d**, shows clearly the formation of silicon-richer particles, probably SiO_2 according to literature [37, 42].

Isolated void formation is observed within the outer oxide layer at 450, 500 and 550°C. The oxide scale formed at 600°C seems to be more compact and only a few voids are observed within the outer layer.

Regarding the nitrided layers, the thicknesses are variable also in these samples. In **Figure 14c** the non-homogeneity of the nitrided layer can be seen clearly. Also in this case, the nitrogen diffusion seems to be influenced by both the microstructures of the alloy and the surface finishing of the samples.

The thicknesses of the oxides formed after 24 and 168 hours are summarized in **Table 2.**

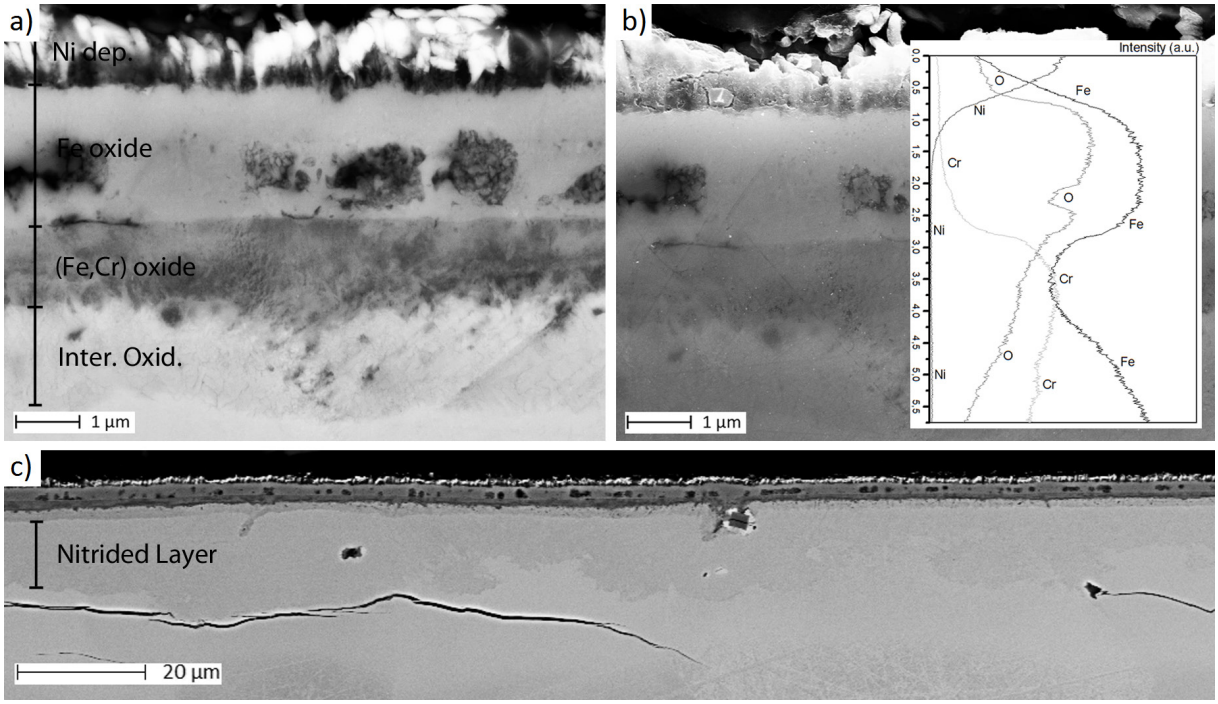

Figure 14. SEM cross-section of 444 after oxidation at 450°C, 168 h in humid air containing 10% H_2O; a) detail of the oxide layer recorded in Back Scatter mode; b) EDS line scan of the oxide layer; c) overview of the oxide layer, Back Scattered Electron image (BSE).

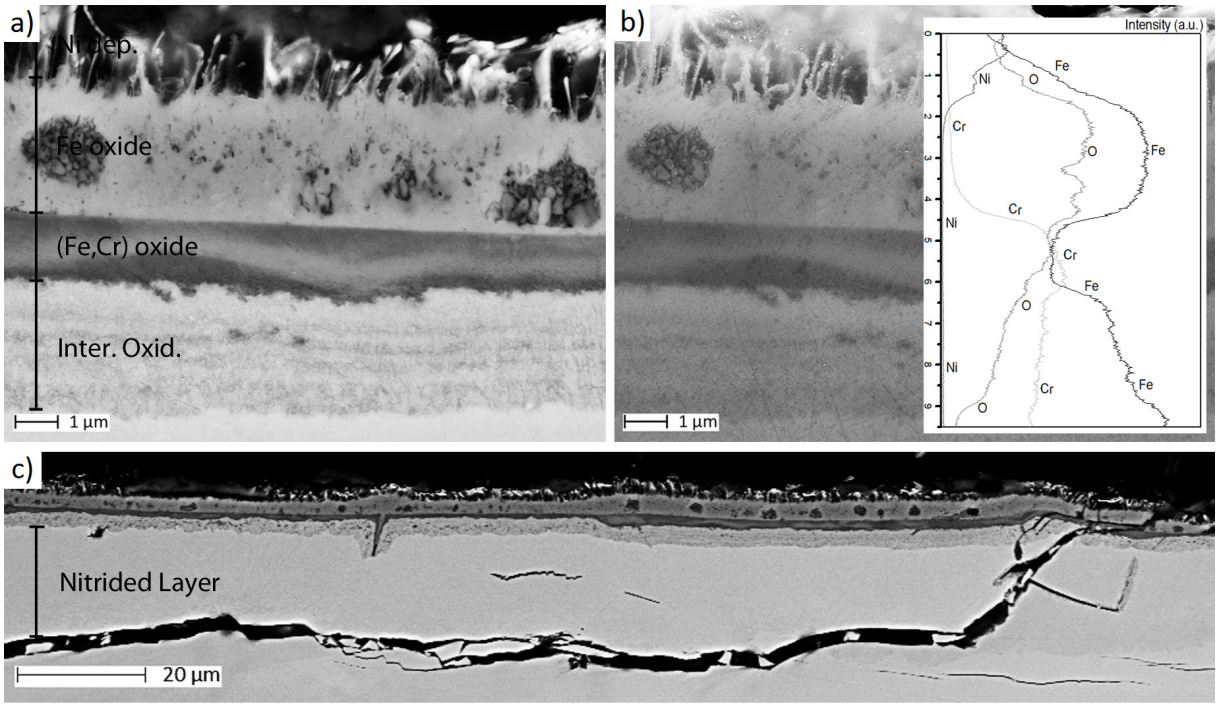

Figure 15. SEM cross-section of 444 after oxidation at 500°C, 168 h in humid air containing 10% H_2O; a) detail of the oxide layer recorded in Back Scatter mode; b) EDS line scan of the oxide layer; c) overview of the oxide layer, Back Scattered Electron image (BSE).

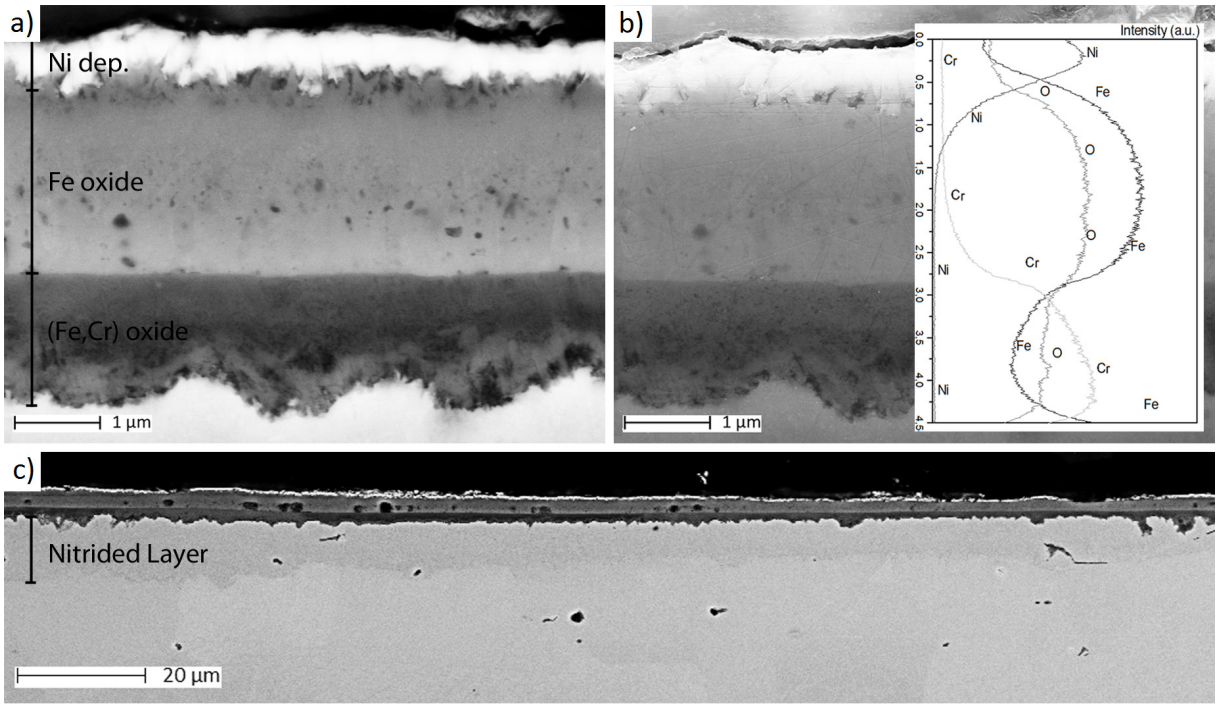

Figure 16. SEM cross-section of 444 after oxidation at 550°C, 168 h in humid air containing 10% H_2O; a) detail of the oxide layer recorded in Back Scatter mode; b) EDS line scan of the oxide layer; c) overview of the oxide layer, Back Scattered Electron image (BSE).

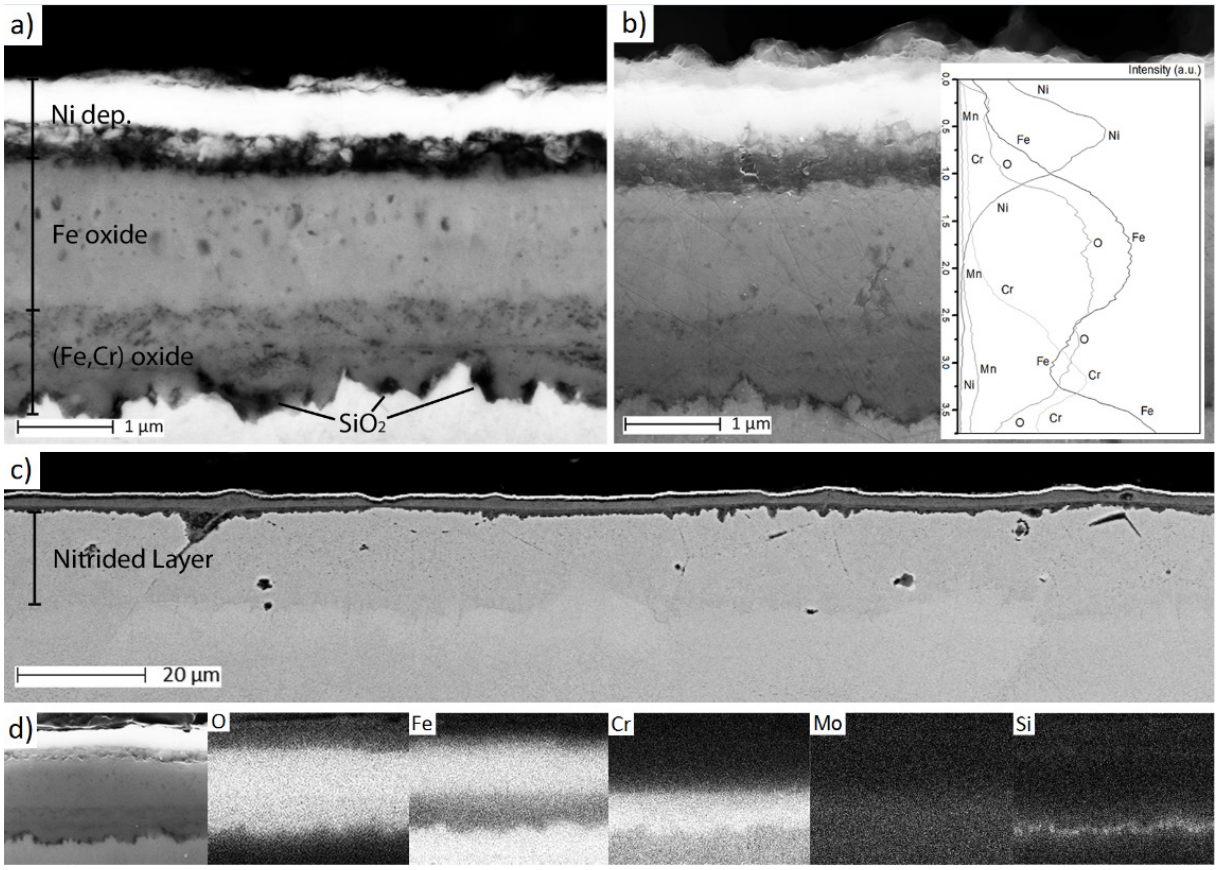

Figure 17. SEM cross-section of 444 after oxidation at 600°C, 168 h in humid air containing 10% H_2O; a) detail of the oxide layer recorded in Back Scatter mode; b) EDS line scan of the oxide layer; c) overview of the oxide layer, Back Scattered Electron image (BSE); d) EDS elemental maps of the oxide layer

Exposure time	24 h				168 h			
Temp. (°C)	**450**	**500**	**550**	**600**	**450**	**500**	**550**	**600**
Oxide (nm)	1400	1700	1450	650	3450	4850	3700	2700
Out.Oxide (nm)	850	1200	950	350	2200	3250	2150	1600
Inn.Oxide (nm)	550	500	500	300	1250	1600	1550	1100
Inter. Oxi. (nm)	n.a.	1200	n.a.	-	1550	3050	-	-
Ratio Inn./Out.	0.65	0.42	0.53	0.86	0.57	0.49	0.72	0.69

Table 2. Thicknesses of the oxides formed on the nitrided material exposed for 24 and 168 hours at different temperatures and 10% H_2O.

4.3 X-Ray Photoelectron Spectroscopy (XPS)

This section presents the results from XPS analysis. The first part deals briefly with the as-nitrided material. The second part presents the XPS depth profiles of the oxide layers formed on as-received and nitrided material after exposure for 24 hours. The samples exposed for 168 hours were not analyzed by using XPS because of the limited timeframe for this work.

4.3.1 Depth Profiling of As-Nitrided Material

The XPS depth profile of as-nitrided 444 was done to evaluate the surface composition of the material after plasma nitriding and sample preparation. The analysis was focused on the first few hundred nanometers of the sample. Aim of this analysis is to quantify the surface nitrogen content of the material after nitriding.

The nitrogen concentration is almost constant for the analyzed profile and decreases only slightly below the surface. The value changes from about 15 at% at the surface to about 13 at% at a depth of 600 nm. The thickness of the full nitrided layer was not determined by using the XPS depth profiling, since the layer is thicker than 10 µm. It was instead estimated by other analytical techniques including SEM cross-section and EDS analysis.

4.3.2 Depth Profiling of As-Received 444 Exposed for 24 Hours

The XPS depth profiles of the as-received 444 after 24 hours oxidation in 10 vol% H_2O humid air are shown in **Figure 18**. The exposure temperatures are 450, 500, 550 and 600°C. The oxide thicknesses are about 30 nm for all the specimens, except the one oxidized at 600°C (about 45 nm).

The results show the formation of an outer iron-rich oxide layer and an inner (Fe, Cr) oxide layer. This tendency can be seen clearly in the graphs excluding oxygen [**Figure 18(a^I-d^I)**], in which a decrease of iron and increase of chromium appears at a few nm below the surface at all the investigated temperatures. This oxide rich in chromium is highly protective and slows down the further oxidation of the underlying material. The almost absence of chromium at the oxide/gas interface can be due to

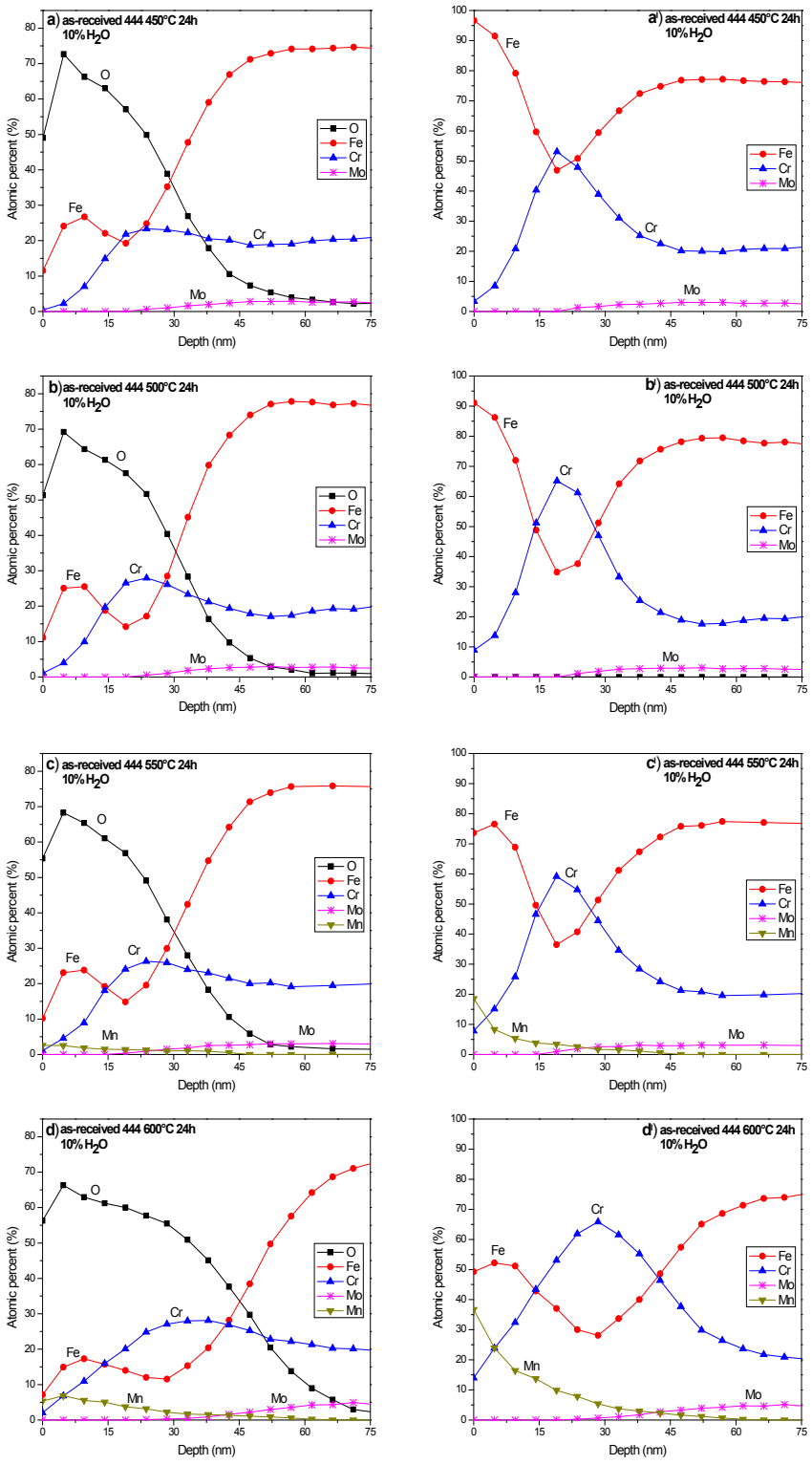

Figure 18. XPS depth profiles of as-received 444 after oxidation for 24 hours in humid air containing 10 vol% H_2O; at a) 450°C; b) 500°C; c) 550°C; d) 600°C. Silicon, carbon and other elements detected mainly at the surface are not shown in these XPS depth profiles. The graphs on the right (a^I, b^I, c^I, d^I) show the profiles of Fe, Cr, Mn and Mo without the oxygen contribution. They may be useful to evaluate the Fe/Cr variation with depths.

the vaporization of chromium species in presence of water vapor, at least at the higher temperatures. As suggested by *Asteman et al.* [32-35] the corrosive effect of water vapor/oxygen mixtures leads to the formation of the volatile species $CrO_2(OH)_2$, which cause chromium depletion in the outer oxide.

Enrichment in manganese at the surface region can be seen for the samples oxidized at 550 and 600°C. The manganese content for the sample heated at 600°C is as high as about 6-7 at% at the surface. Regarding molybdenum content, it seems to increase inwards from the inner/outer oxide interface. Silicon content is observed at the oxide surface, where it decreases quickly within the first few nanometers. Small amounts are detected again within the outer oxide layer at all exposure temperatures. The silicon content is not shown in **Figure 18**, since its weak amount.

In conclusion, the results confirm the formation of a thin oxide layer on all as-received 444 specimens exposed for 24 hours. The rather limited oxidation indicates that the oxide is still protective at all temperatures. The thickness of the oxide formed is more or less the same on all the samples, with the exception of the one exposed at 600°C. In this case the oxide layer is slightly thicker but still in the same order. This result can be explained as the higher oxide growth rate at higher temperature.

4.3.3 Depth Profiling of Nitrided 444 Exposed for 24 Hours

Figure 19 shows the depth profiles of the nitrided 444 exposed for 24 hours in humid air containing 10 vol% H_2O. Also in this case the exposure temperatures are 450, 500, 550 and 600°C. The oxide thickness changes from about 230 nm (sample oxidized at 600°C) to about 2910 nm (sample oxidized at 500°C). The other two samples exposed at 450°C and 550°C have oxide thickness, 1520 and 1410 nm respectively.

As seen in **Figure 19(a-d)**, an outer layer of pure iron oxide and an inner layer richer in chromium always form in the oxide. At all temperatures chromium is not found in the outer oxide layer. Similar to the as-received material, the absence of chromium in the outer oxide layer is due to the corrosive effect of water, that reacts with chromium to form the volatile species $CrO_2(OH)_2$ [32-36].

The worst oxidation resistance for the nitrided 444 is found at 500°C. This result agrees with the results obtained by *Cao and Norell* [41] about the oxidation of nitrided austenitic stainless steels 304L and 904L. At this temperature the chromium depletion is particularly visible and the thickness of the outer iron oxide layer is about 1900 nm. At 500°C the diffusivity of chromium is lower than at higher temperature but at the same time the oxide growth is significant. Although at 450°C the chromium diffusivity is lower than at 500°C, the restrained growth rate shows to be the limiting factor for the oxide growth. By increasing the temperature, both of chromium diffusivity and oxide growth rate become higher.

Similar to the as-received material, a significant enrichment of manganese towards the surface is found for the nitrided samples heated at 600°C. Manganese is not detected at the other temperatures. Molybdenum cannot be detected at the outer oxide layer. It starts to increase from the interface of outer and inner oxide. The nitrogen profiles for the nitrided samples after exposure are of interest. No nitrogen can be observed at the outer oxide region. It seems to increase inwards from the interface of inner and outer oxide at all the exposure temperatures. It increases quickly at 600°C and more slowly at other temperatures. The nitrogen content, evaluated down to the analysis depth, is about 10-11 at% for all the samples. Silicon content is observed at the oxide surfaces of nitrided samples exposed at all temperatures. The content decreases quickly within the first few nanometers. Small amounts are detected again within the inner oxide layer at all exposure temperatures, except within the thin oxide scale formed at 600°C. The silicon content is not shown in **Figure 19** since the amount is low.

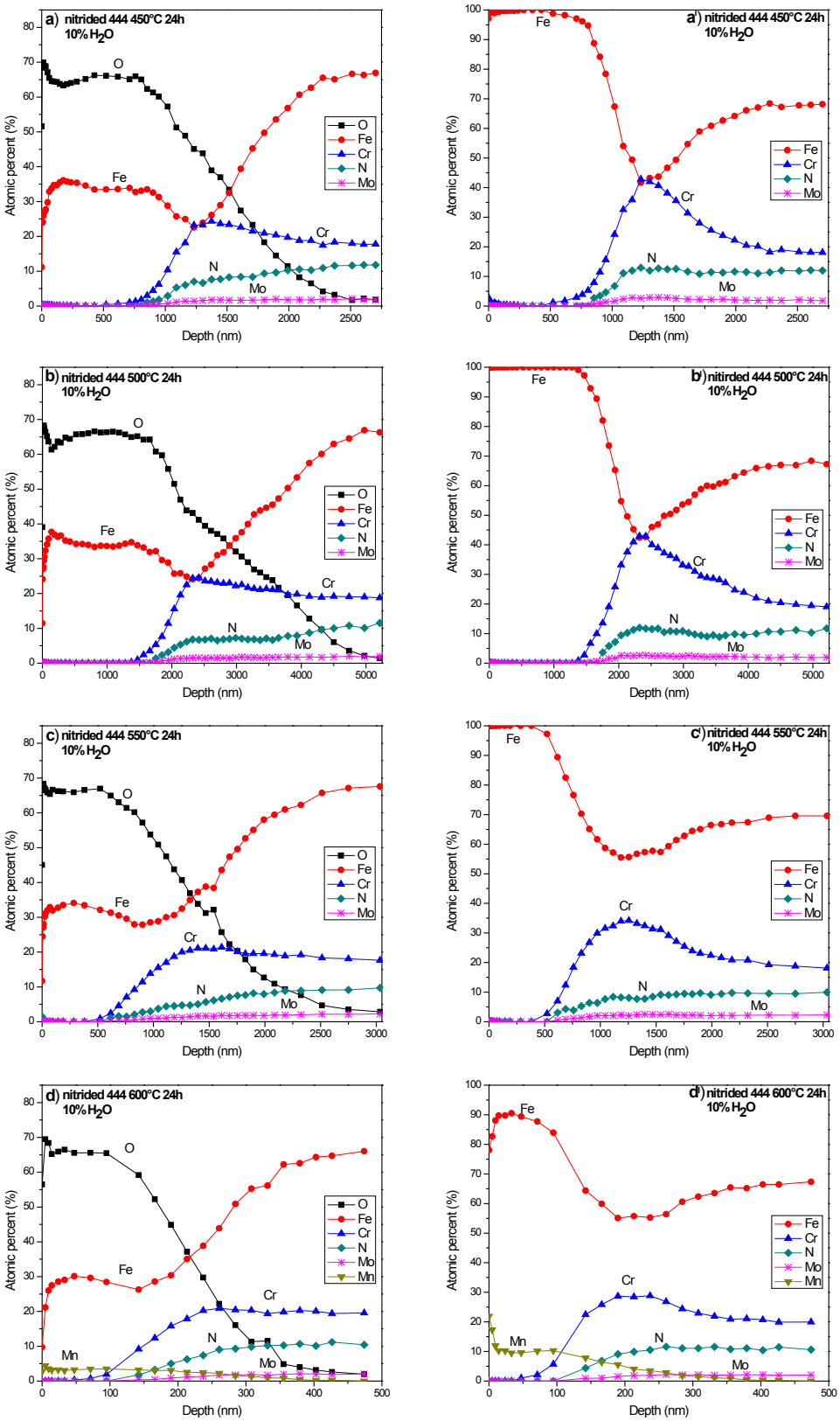

Figure 19. XPS depth profiles of nitrided 444 after 24 hours exposure in humid air containing 10 vol% H_2O; at a) 450°C; b) 500°C; c) 550°C; d) 600°C. Silicon, carbon and other elements detected mainly at the surface are not shown in these XPS depth profiles. The graphs on the right (a^I, b^I, c^I, d^I) show the profiles of Fe, Cr, N, Mn and Mo excluding oxygen contribution.

	As-received 444				Nitrided 444			
Temp. (°C)	**450**	**500**	**550**	**600**	**450**	**500**	**550**	**600**
Oxide (nm)	30	30	30	45	1520	2970	1410	230
Out.Oxide (nm)	-	-	-	-	1000	1880	750	126
Inn.Oxide (nm)	-	-	-	-	520	1090	660	104
Ratio Inn./Out.	-	-	-	-	0.52	0.58	0.88	0.83

Table 3. Oxide thickness for material as-received and nitrided oxidized at different temperatures for 24h in 10% H_2O.

Table 3 summarizes the oxide thicknesses obtained after 24 h exposure for the as received and nitrided samples. The oxide formed on the nitrided 444 is 50-100 times thicker than on as-received 444 for the exposure temperatures between 450 and 550°C. Nitrogen seems to be less detrimental at higher temperatures. At 600°C, the oxide formed on nitrided 444 is only 5 times thicker than on as-received 444. Nevertheless, the oxidation rate at this temperature is considerably lower. Moreover, the thickness ratio between the inner and the outer oxide increases with increasing the exposure temperature. This can be explained by the higher chromium diffusivity at higher temperatures, which facilitates the formation of the protective oxide.

4.4 X-Ray Diffraction (XRD)

This section presents the XRD results obtained from as-received and nitrided 444, before and after exposure. The samples were analyzed by both normal θ/θ geometry and grazing angle incidence (3°) XRD. The grazing angle incidence X-Ray diffraction is useful for the samples which are less oxidized, since it has smaller information depth. Purpose of the XRD analysis is to identify the phases formed after nitridation and oxidation. In this work the analysis is only qualitative. However, some correlations between pattern intensity and oxide thickness will be clarified.

4.4.1 As-Received and As-Nitrided Material

Figure 20 gives the XRD pattern from the as received 444 and as-nitrided 444. The XRD pattern of the as-received sample is characterized by the presence of two well-defined peaks attributed to the ferritic phase. The third peak located at higher 2θ angle is a K_β signal of the ferritic phase.

After plasma nitriding, the XRD pattern is more difficult to explain. In this case four peaks are visible. The most intense peak detected is the ferritic phase. The broadening of the peak is associable to the presence of a large amount of nitrogen inside the ferritic structure. This effect is due to the presence of chromium within the ferritic structure [17]. Chromium has a high affinity with nitrogen and carbon and forms strong bonds with them. In the alloy, it attracts nitrogen and form short-range ordering, resulting in the saturation of nitrogen in the ferritic structure.

According to literature, this amount of nitrogen leads to the formation of an S^α phase, which is considered to be a supersaturated solid solution of the ferritic phase [11, 15]. The nitrogen content causes expansions and distortions inside the ferritic structure and consequently high stresses. The broad peak at higher 2θ angle is probably an overlap of more peaks. In accordance with literature

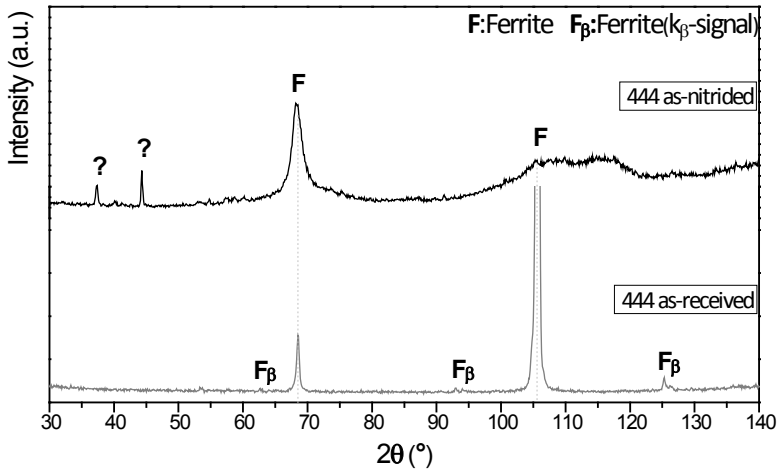

Figure 20. X-Ray diffraction pattern of as-received and nitrided 444 stainless steel.

[11, 16, 17], this can partly be associated with the presence of a saturated solid solution of nitrogen inside the ferritic phase.

The low temperature of the plasma nitriding may explain the absence of well-defined peaks from Cr nitride phases. Indeed, the low temperature, about 400°C, is not able to promote the precipitation and growth of nitrides [11-14]. The nitrogen remains in solid solution into the ferrite lattice. About the two less intense peaks located at 37.3 and 44.3°, the identification of the phase has not been possible at the current stage.

4.4.2 Oxidation of 444 Stainless Steel

4.4.2.1 As-Received Material

Figure 21 shows the XRD patterns of the oxide layers formed on the as-received 444 at different temperatures and exposure times. The oxide layers formed on the as-received material are particularly thin. For this reason, grazing angle incidence XRD technique was used in order to focus the analyses on the surface.

After both 24 and 168 hours exposure, formation of a thin corundum-type oxide at all temperatures can be noted. The corundum-type oxide corresponds to a α-Fe_2O_3 (hematite). No other oxidation products can be detected at all temperatures investigated. Weak peaks located at 57,9 and 63,9° are observed at the highest temperature 600°C for longer exposure time. They are less clear for the short exposure at the same temperature. The corresponding phase identification is difficult. Considering that they appear only at highest temperature studied, carbide precipitation might be possible. It seems the effect of the exposure time on the phase is not as important as temperature.

Although quantification of the oxide formed on the material was not done, it is clear that the oxidation of the as-received 444 is slight, and less dependent on the exposure time and temperatures investigated. According to the XPS depth profiles of the 24 hours exposure, the oxide thicknesses for the as-received material are in the order of 30 nanometers.

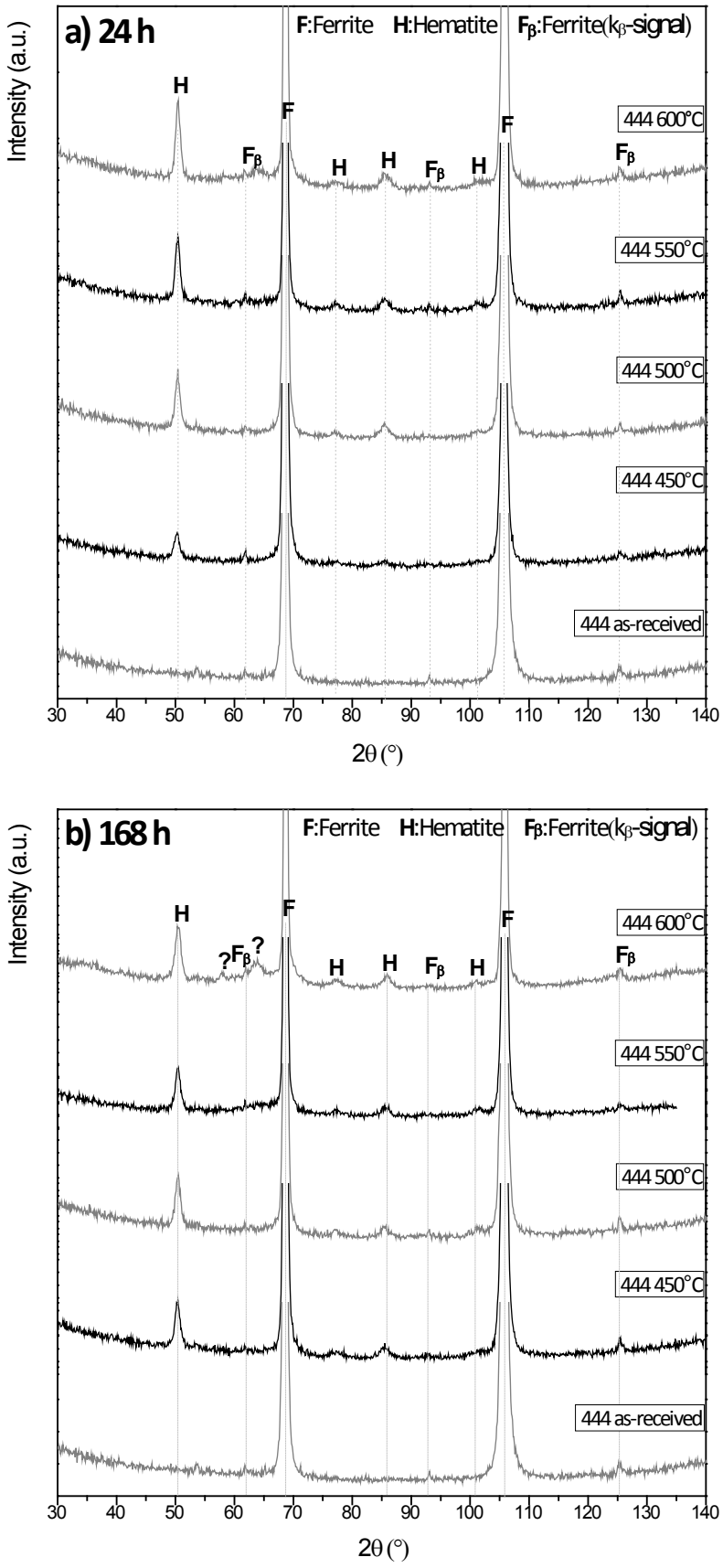

Figure 21. Grazing angle incidence (3°) X-ray diffraction patterns from as-received 444 oxidized for a) 24h and b) 168h. The X-ray diffraction pattern of the 444 as-received is added as reference.

4.4.2.2 Nitrided Material

The XRD patterns of the nitrided samples after oxidation at different temperatures and exposure times are shown in the **Figure 22**. XRD pattern of the as-nitrided sample was added as reference. The XRD analysis after an exposure time of 24 hours **(Figure 22a)** indicates the presence of mainly corundum-type oxide, corresponding to α-Fe_2O_3 (hematite), with traces of spinel-type oxide, possibly as magnetite (Fe_3O_4), and precipitation of CrN. At the highest temperature of 600°C the peaks of magnetite cannot be detected, even with a grazing angle incidence. This can be due to the thinner oxide layer formed during exposure at 600°C.

According with XPS analysis, general decrease of the oxidation is observed at exposure temperatures higher than 500°C. Moreover, the FWHM (full width at half maximum) tends to decrease with the increase of temperature and time. At higher temperatures, the ferrite peaks become narrow and approach the ideal diffraction lines. This behavior is related to the nitrogen removal from the ferritic structure. In this case the nitrogen mobility is higher and tends to react with Cr to form nitrides.

Chromium nitrides can be detected at all temperatures. The broader peaks at 450°C suggest the formation of very fine precipitates. By increasing the temperature, CrN peaks become narrower, due to the precipitate growth.

The XRD patterns obtained after an exposure time of 168 hours **(Figure 22b)** show the formation of a thicker oxide layer. Mainly hematite (Fe_2O_3), magnetite (Fe_3O_4) and chromium nitrides (CrN) are identified. Comparison of the patterns obtained at different temperatures indicates a thicker oxide layer at 500°C. At this temperature, the main peaks for hematite and magnetite are particularly intense, and also the secondary peaks of both the phases can be detected. The magnetite peaks are well defined at 450°C. As well in this case, the intensity of the main peak equals to the intensity of the main hematite peak. At the higher temperatures similar behavior as for 24 hours exposure is observed. No magnetite can be detected at 600°C for both 24 and 168h exposure. In addition, a new phase appears at this temperature. This new phase corresponds to another chromium nitride, Cr_2N. The precipitation of this nitride takes place only at highest temperature and longest exposure time in this study. It seems to be an equilibrium phase. Nevertheless further study is needed to better understand the phenomenon.

Regarding the FWHM of the main ferritic peak similar to the 24h exposure, it also decreases with increasing temperatures. Furthermore, the FWHM values measured from the samples exposed for 168 hours is smaller than those measured for the 24 hours exposures. The longer exposure time allows the removal of more nitrogen from the ferritic structure and consequently the width of the peak decrease. The narrower and more intense CrN peaks suggest an increase of the grains sizes of the precipitate, particularly visible at the highest temperature.

After a quick comparison between the XRD patterns of the as-received material and nitrided one, the effect of nitrogen uptake on oxidation of 444 stainless steel can be confirmed. The oxide layers for the nitride samples are always thicker than those formed on the as-received samples. This is consistent with the XPS results and SEM observations. Only hematite phase can be detected on the as-received samples, at all the temperatures and exposure times. However, both hematite and magnetite can be observed on the nitrided samples with the exception of 600°C.

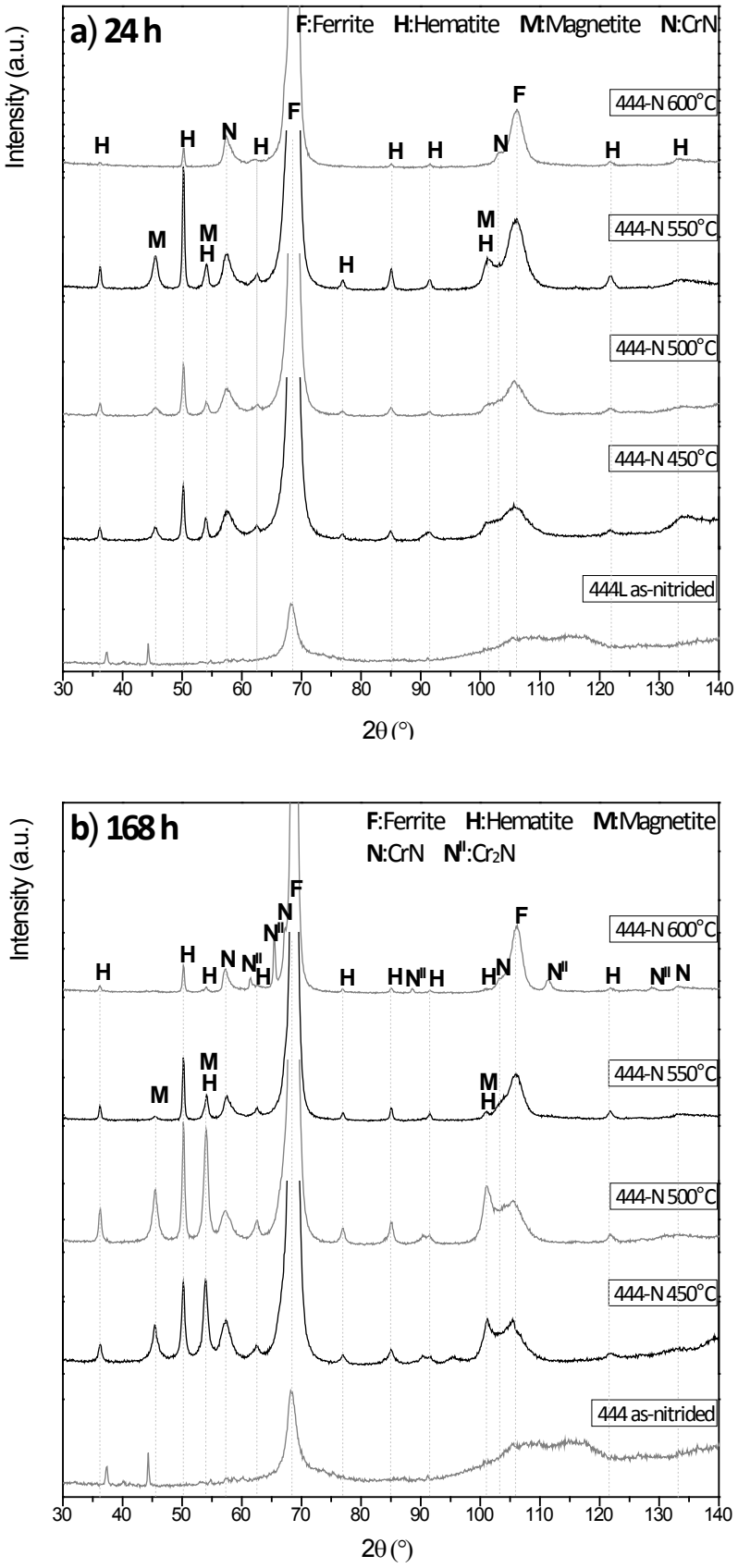

Figure 22. X-ray diffraction patterns from nitrided 444 oxidized for a) 24h and b) 168h. The X-ray diffraction pattern of the nitride 444 is added as reference.

Chapter 5

Discussion

The chapter consists of two parts. The first part focuses on the oxidation behavior of nitrided AISI 444 ferritic stainless steel in humid air by considering the effect of the nitrogen uptake and water vapor on the high temperature corrosion. The influence of temperature and exposure time on the corrosion resistance and the oxide formed will be discussed.

The second half of the chapter will compare the results obtained in this present work for the oxidation of nitrided 444 ferritic stainless steel with those reported in the previous studies for the nitrided 304L and 904L austenitic stainless steels, exposed in the same conditions.

5.1 Oxidation of Nitrided 444 Ferritic Stainless Steel in Humid Air

The discussion of the results will cover three aspects: effect of nitrogen uptake in water vapor on the oxidation behavior of 444; characterization of the oxide layers; dependence on temperature.

5.1.1 Effect of Nitrogen Uptake on the Oxidation of 444 in Water Vapor

The oxidation resistance of the AISI 444 ferritic stainless steel, in the temperature range 450 to 600°C, is clearly deteriorated by the plasma nitriding performed at 400°C. The results consistently show the formation of oxides 50-100 times thicker on the nitrided samples than those observed on as-received material. At 600°C the effect seems less strong, but also in this case the oxide scale formed on the nitrided material is 5 times thicker than on the as-received.

As expected, the oxide scales formed after 24 and 168 hours of exposure in humid air containing 10% H_2O are composed of an outer iron oxides and an inner iron-chromium oxide. The corrosion mechanism of the stainless steel is presumably the same as that reported in the literature for the environment containing water vapor [32-36]. The formation of chromium volatile species removes chromium from the alloy and leads to the formation of a poor protective oxide scale. Both XPS depth profiles and elemental EDS line scans showed the formation of an outer iron-oxide layer and an inner chromium-richer oxide for all the nitrided samples analyzed. Also the XPS depth profiles performed on the as-received coupons after oxidation show a general enrichment in chromium below the outer Fe oxide layer under all the exposure conditions.

The aim of this work is to understand how the nitrogen uptake and the phases formed affect the oxidation of the AISI 444 ferritic stainless steel. It is important to consider the availability of chromium at the surface region to form the protective oxides. The XRD pattern of the as-nitrided material suggests the formation of an expanded ferrite phase (S^{α}), due to the large amount of nitrogen entrapped into the ferritic lattice [16]. Formation of chromium nitrides is not observed in

the as-nitrided material. The low temperature of the plasma nitriding, about 400°C, does not allow precipitation of Cr nitrides. In addition to the expanded S^{α} phase, further peaks detected in the XRD pattern suggest the presence of other phases due to the plasma nitriding. The identification of these phases was not possible in this study.

The formation of CrN was observed in all the samples oxidized at all exposure temperatures. It is well known that as soon as the chromium presents in solution precipitates into the nitrides, it is no longer available for the formation of a protective oxide scale [7]. However, the higher oxidation rate of the nitrided 444 compared to that of the as-received 444, cannot be explained by considering only the Cr-nitrides precipitation. Although at higher exposure temperatures more CrN precipitates than at lower exposure temperatures, the oxidation of the material is definitely weaker at 600°C.

It is believe that the presence of a large amount of nitrogen inside the expanded ferrite phase (S^{α}-phase), due to the plasma nitriding, affects the corrosion resistance of the alloy as well. As reported in literature [43-44], the high affinity between chromium and nitrogen leads to the formation of short-range ordering of N and Cr, associated with large local distortions around Cr atoms. According to a study, regarding the oxidation of nitrided austenitic stainless steels by *Cao and Norell* [41], this short-range ordering between N and Cr decreases the activity of chromium, preventing the diffusion of Cr towards the surface and consequently the formation of the protective chromium-rich oxide.

The accelerated oxidation of the nitrided 444 compared to the as-received 444 may be explained by considering both the presence of the S^{α}-phase formed during plasma nitriding and the CrN precipitates developed during the exposures. At higher temperatures, the more extensive precipitation of Cr-nitrides leads to a greater transfer of nitrogen from the ferritic lattice. It might be possible that the chromium remained after the precipitation of Cr-nitrides is more available at higher temperatures and it can longer maintain the protective oxide.

5.1.2 Characterization of Oxide Layers

The oxide scales formed in humid air containing 10% H_2O on the nitrided 444 ferritic stainless steel adheres strongly to the substrate and appears generally optically smooth. SEM images show preferential oxidation at the grain boundaries and some grains with particular lattice orientations. Moreover, samples exposed at low temperatures exhibits a large number of whiskers evenly distributed over the surface. At higher temperatures irregular pebble-like crystallites with about 0.2 μm in size are observed.

The SEM cross-section images indicate the oxide scales formed are composed of two distinct layers at all the temperatures investigated. These two layers are separated by a very sharp and planar boundary, as seen clearly in the images taken by using Back Scattered mode. XRD analyses reveal that the oxides formed on nitrided 444 samples consist mainly of corundum-type oxide, hematite (Fe_2O_3) and spinel-type oxide, possibly magnetite (Fe_3O_4). As expected, formation of wüstite is not observed at 600°C since the presence of chromium decreases its stability [24]. At this temperature, the presence of magnetite is not detected neither. The thinnest oxide layer formed at the highest exposure temperature may explain the absence of the magnetite peak on the XRD pattern. Even if some magnetite could be formed during the exposure, the limited amount made it difficult to be detected by using XRD. The formation of Cr-nitrides phase is observed on the XRD patterns at all the exposure temperatures. Both the XPS depth profiles of the samples oxidized for 24h and the elemental EDS line scans performed on the cross-sections of the same sample confirm the formation of an outer pure iron-oxide layer and an inner (Fe,Cr)-oxide layer.

Though the weight gain was not examined in this study, the appearance and composition of the thin and thick oxides formed clearly indicate breakaway corrosion, after 24h of exposure at all

temperatures. The outer oxide layer has a lower chromium content with formation of Fe_2O_3/Fe_3O_4. This behavior can be understood in terms of the vaporization of chromium oxide hydroxide in presence of environments containing water vapor [32-36].

Turning to the results obtained by using XPS depth profiling, significant enrichment of manganese is observed in the outer oxide layer for the sample oxidized at 600°C. Many studies [32, 35, 37, 40, 45] report the accumulation of manganese at the external surface. *Issartel et al.* [45], who studied the isothermal oxidation of ferritic 4509 steel in the range of 800-100°C, suggested that manganese can increase the corrosion resistance of the material by forming manganese chromite that hinders the chromia scale volatilization under dry condition. *Helcomb et al.* [40] observed a similar behavior also for oxidation of Ni-Cr alloys at 700 and 800°C, under wet conditions. In this case, the formation of a $MnCr_2O_4$ oxide scale reduces the volatilization of the $CrO_2(OH)_2$. In this present work, the effects of manganese on the oxidation of ferritic 444 stainless steel have not been followed out.

Molybdenum and nitrogen start to increase from the interface of outer and inner oxide at all temperatures. *Shu et al.* [46] observed a beneficial effect of molybdenum on the high temperature oxidation resistance of the ferritic stainless steel. They found that the higher molybdenum content in AISI 444 compared to that in AISI 441 promotes the formation of Laves phase (Fe_2(Nb, Mo)). These phases located at the triple boundaries were suggested to inhibit the bulk diffusion of Fe and Cr cations.

Alloying element silicon was detected by using elemental EDS line scans and elemental EDS maps. Higher silicon content is observed within the inner oxide layer at all temperatures in this study. For the longer time exposure at 600°C, significant increase of silicon is observed at the interface between oxide scale and alloy, where it seems to precipitate as broad particles. This is clearly visible on the EDS maps of the Si channel. Several studies [37, 42, 45, 47] report the formation of silicon phases at the interface between oxide and alloy. *Brady et al.* [37] observed the formation of a silica layer at the alloy-oxide interface of AISI 430 exposed for 24h at 800°C in presence of 10% H_2O. *Wouters et al.* [42] also found the presence of a thick and compact silica layer between the steel substrate and the chromia scale after oxidation of Fe-15Cr-O.5Si grade at 950°C for 8h in environment containing 150 mbar H_2O. The precipitation of a SiO_2 layer at the internal interface is due to the high silicon affinity to oxygen that permits its internal oxidation [45]. It was reported that the presence of a silicon layer between the chromia scale and the steel decrease the oxidation rate and leads to a slower post-breakaway growth [42]. In the present work, no silica film has been detected after oxidation in environment containing 10% H_2O but some isolated silica particles are observed on the cross section of the sample oxidized at 600°C for 168h (**Figure 17a**). It should be pointed out that these studies [37, 42, 45, 47] were all performed at 800°C or higher. Thus at temperatures where the diffusivity is much higher.

5.1.3 Dependence on Temperature

The analyses performed on the nitrided AISI 444 ferritic stainless steel after oxidation for 24 and 168h in environment containing 10% H_2O show that generally at lower exposure temperatures the oxidation is more severe than at higher temperature. XRD analysis confirms the formation of both hematite and magnetite in the temperature range 450-550°C, while only hematite can be detected at 600°C. The thickest oxide layer is observed at 500°C for both the exposure times.

At this temperature the thickness of the oxide scale measured on the SEM cross-section is about 1.7 µm after 24h exposure and about 4.9 µm after 168h. The thinnest oxide layer is observed at 600°C; about 0.7 µm after 24h exposure and 2.7 µm after 168h. CrN peaks become narrower and sharper at this temperature. For the longer exposure time, precipitation of both Cr_2N and CrN is observed. At 450°C the thickness of the oxide scales formed is 1.4 µm and 3.5 µm for 24h and 168h respectively. The oxide formed at 550°C is 1.5 µm for 24h and 3.7 µm for 168h.

As show in **Table 3,** the thickness ratio between the inner (Fe,Cr)-oxide layer and outer pure Fe-oxide layer is lower for the scales formed at low temperatures than for those formed at higher temperature. The lowest value is found for the oxide scale formed at 500°C. At this temperature the growth of the outer oxide seems to be greater than at the other temperatures and the scale is mainly formed by iron oxides.

The lowest oxidation rate of the sample exposed at 600°C can be explained as follows. According to literature [38, 48], the diffusivity of chromium in the α-Fe increases by increasing the temperature. The higher diffusivity of chromium at 600°C allows a better supply from the substrate toward the oxide and replace the chromium loss by vaporization [36]. From another hand, *Ani et al.* [48] observed that the minimum chromium concentration required to form an external chromia scale and to maintain the scale in dry and humid air decreases with an increase of temperature, which also facilitates the early formation of protective Cr-rich oxide at higher temperatures.

However, XPS depth profile confirms a lower Cr/Fe ratio in the inner oxide layers formed at higher temperature. The growth of the outer iron-oxide layer is slower on the sample exposed at 600°C. The results are in disagreement with what would be expected. The higher Cr/Fe ratio in the inner oxide layer formed at lower exposure temperatures suggest the formation of more protective (Fe,Cr) oxide layers.

The elemental EDS line scans performed on the cross-sections of the samples oxidized for 168h show higher Cr/Fe ratio for the inner oxide layers formed at higher temperature, confirming the formation of more protective oxides at these temperatures. The presence of an oxygen diffusion layer beneath the oxide at 450 and 500°C, as seen on the SEM cross-sections images and elemental EDS line scans, is also of interest. In particular at 500°C, **Figure 15a**, the layer is considerably thick. Although it cannot be considered as part of the oxide scale due to the low oxygen concentration, the presence of internal oxidation in the material underlying the oxide can be also seen as a signal of the most severe oxidation at 500°C and the poor protectiveness of the inner oxide layer.

5.2 Oxidation of Nitrided Ferritic and Austenitic Stainless Steels in Humid Air

This section will present a comparison between the results obtained during this project regarding the oxidation of the nitrided 444 stainless steel and the results obtained by *Cao and Norell* [41] in previous studies regarding the oxidation of the nitrided 304L and 904L austenitic stainless steels.

5.2.1 Results Obtained in Previous Studies

Cao and Norell [41] investigated the role of nitrogen uptake in oxidation of 304L and 904L austenitic stainless steels. The chemical compositions of the two alloys are listed in **Table 4**. The oxidation of the two stainless steels was examined by exposing both as-received and nitrided samples. The samples were plasma nitriding at about 400°C using two different N_2 partial pressure and treatment duration. For the purposes of this comparative investigation, only the results regarding the samples plasma nitrided for 24h in 6% N_2 partial pressure will be considered. The exposures were carried out in the same condition as the current study.

Cao and Norell found that plasma nitriding at about 400°C deteriorates the oxidation resistance of both the austenitic steels studied in the temperature range 450-600°C. As can be seen in **Table 5**, the deterioration was very marked for the 304L. The oxide scales were 70-100 times thicker than on the

	Fe	C	Mn	Cr	Ni	Mo	Si	S	P	N	Cu	Ti
304L	Bal.	0.019	1.63	18.25	8.05	0.43	0.28	0.001	0.028	0.072	0.33	0
904L	Bal.	0.011	1.62	20.3	24.26	4.37	0.33	0.001	0.023	0.054	1.41	0.007

Table 4. Chemical composition of AISI 304L and 904L austenitic stainless steels.

as-received 304L. Also the nitrided 904L was more oxidized than the as-received 904L but the oxide scales were only 2-5 times thicker. The XRD results showed the formation of expanded austenite phase on the surface of both the as-nitrided alloys. Precipitation of chromium nitrides was not detected on the as-nitrided samples.

XPS and AES depth profiles showed the general formation of an outer Fe-oxide layer and an inner (Fe,Cr)-oxide layer on all as-received and nitrided samples oxidized for 24h, except for the 904L exposed at 500°C. In this case no clear enrichment of chromium was found. Enrichment in manganese was observed in the outer oxide layer for both the as-received and nitrided samples of 304L oxidized for 24h at 600°C. The XRD analyses of the nitrided 304L samples oxidized for 24 and 168h showed formation of mostly hematite and spinel phase (possibly as magnetite) at all temperatures. Only hematite was detected for the nitrided 904L samples exposed for 24 and 168h.

Precipitation of CrN was detected on the 304L samples at all the exposure temperatures. The XRD patterns of the samples showed the presence of a weak and broad CrN peak at 450°C. The CrN peaks became narrower and more intense by increasing temperature, consistent with the increase of nitrides precipitation and grain size. Regarding the 904L, the most intense CrN peak was found at 500°C, whereas no CrN peaks were detected at 450 and 600°C.

The decomposition of the S-phase was observed both for 304L and 904L samples during oxidation at higher temperatures. At higher temperatures and longer times of exposure, the diffraction peaks of the S-phase were shifted to higher 2θ angles and partially merged into the austenite peak. In 304L formation of bcc-phase during oxidation was observed. At 550 and 600°C the S-phase was almost completely transformed to bcc-phase, fcc-phase and CrN. For 904L, formation of bcc-phase was not detected.

Time	**Temperature**		**450°C**	**600°C**	**450°C**	**500°C**	**550°C**	**600°C**
	Nitriding		**none**	**none**	**X**	**X**	**X**	**X**
24h	**304L**	**XPS/AES (nm)**	28	37	2500	4500	470/ 4000	560/ 2600
	904L	**XPS/AES (nm)**	32	50	150	210	135	110
	444	**XPS (nm)**	30	45	1520	2970	1410	230
		SEM (nm)	-	-	1400/ n.a.	1700/ 1200	1450/ n.a.	650
168h	**444**	**SEM (nm)**	-	-	3450/ 1550	4850/ 3550	3700	2700

Table 5. Oxide thicknesses for as-received and nitrided austenitic 304L, 904L (data from [41]) and ferritic 444 stainless steels oxidized for 24h and 168h in humid air containing 10% H_2O. Regarding the austenitic 304L, there is the formation of both thin and thick oxide layers at 550 and 600°C. Regarding the ferritic 444, the two values measured on the SEM cross sections are related to the thickness of the oxide scale (first one) and to the thickness of the internal oxidation layer (second one).

5.2.2 Oxidation in Humid Air for Alloys 444, 304L and 904L after Nitridation

The results obtained in this study for nitrided ferritic stainless steel 444 oxidized in humid air containing 10% H_2O will be compared to the results obtained by *Cao and Norell* [41] for nitrided austenitic stainless steels 304L and 904L. The austenitic stainless steels are generally more used for applications at high temperatures since they are characterized by superior oxidation resistance. The addition of nickel in these grades transforms the iron from a ferritic to an austenitic phase, which has FCC structure and is more stable at high temperatures. It has also been suggested that nickel influences the adhesion and mechanical properties of the scale, and retards the breakaway transformation [6, 24].

Looking at the chemical composition of the three alloys, **Table 1 and 4**, it can be seen that the alloying element content is higher for the 904L. Particularly, chromium, nickel and molybdenum contents are higher in this alloy. Consequently, the 904L shows an improved oxidation resistance compared to the others two alloys analyzed. Also the detrimental effect of the nitridation on oxidation is less serious for 904L than for 304L and 444. Both nickel and molybdenum contents stabilize the S-phase and decrease the Cr-nitrides precipitation during the exposures [41]. Although the 904L shows the best oxidation resistance in the temperature range 450-600°C, the high cost limits its use. The lower alloying element content in austenitic 304L and ferritic 444 stainless steels compared to 904L austenitic grade makes these two alloys cheaper and more interesting for the application in exhaust after-treatment systems.

The oxidation behavior of the ferritic 444 and austenitic 304L after nitriding appears rather similar. For both alloys the detrimental effect of nitridation on the oxidation resistance is clear. The oxide scales formed on nitrided 444 are about 50-100 times thicker than on as-received 444 and on the nitrided 304L about 70-100 times thicker than on as-received 304L. The strong effect of nitridation on the oxidation of ferritic 444 and austenitic 304L can be explained considering both the formation of expanded phases supersaturated of nitrogen and the further precipitation of Cr-nitrides during the exposures. These two factors reduce the activity of chromium, preventing its diffusion from the alloy toward the surface and consequently the formation and maintenance of the protective oxides [41].

The oxide scales formed on the nitrided samples are generally smooth and quite homogenous in thickness for 444 grade. Regarding 304L grade, the oxides formed are less homogeneous in thickness. Areas of thin and thick oxides are observed in this alloy. XPS depth profiles on nitrided 444 and AES/XPS depth profiles on nitrided 304L show a general deterioration of the oxidation resistance at low temperatures. The thickest oxide scales are observed for both the alloys after exposure at 500°C, which is about 4.5 µm for 304L and 3 µm for 444. The improved oxidation resistance is observed at the highest exposure temperature, both for 444 than 304L. At this temperature the oxide formed on 444 is particularly thin, about 0.23 µm (XPS depth profile). For the 304L, the values obtained for thin and thick oxides are 0.56 and 2.6 µm respectively (AES depth profiles).

It is thus concluded that 444 ferritic stainless steel has lower oxidation rate and more homogeneous oxide thickness than 304L for 24 hours exposures. This may be explained by considering the differences of the composition and microstructure of the two alloys. The higher chromium diffusivity in ferritic than in austenitic stainless steels may allow a quicker supply of chromium from the substrate to the oxide, improving the oxidation resistance of the ferritic grade [35-36].

The less extensive oxidation at higher temperatures can be explained for both the alloys as an effect of the larger nitrogen transfer from the expanded phases, by which more chromium becomes available for the formation and maintenance of the protective oxide.

Chapter 6

Conclusions

Expanded ferrite supersaturated with nitrogen, S^{α}-phase is formed on the surface of the as-nitrided 444 ferritic stainless steel. Precipitation of Cr-nitrides is not observed after the plasma nitriding, since the treatment temperature is too low.

The effect of nitridation on the oxidation resistance of the ferritic 444 is particularly detrimental in the range of 450 to 550°C. The oxide scales formed on the nitrided material are 50-100 times thicker than on the as-received material. At 600°C the effect is less marked and the oxide scale formed on the nitride sample is 5 times thicker than on the as-received material. The precipitation of Cr-nitrides detected after exposures at all temperatures together with the presence of the S^{α}-phase, which presents short-range ordering between Cr and N, seems to reduce the activity of Cr that is no longer available to form a protective oxide. The less oxidation of nitrided samples at higher temperatures can be explained by the lower of nitrogen content in ferritic expanded phase. With less nitrogen the chromium remained is more available to form and maintain the protective oxide.

The oxide scales formed on the nitrided 444 samples are composed of two layers separated by a very sharp and planar boundary. The oxides are mostly corundum-type (hematite) and spinel-type at all temperatures, except at 600°C. At this temperature only hematite can be detected by XRD. Precipitation of CrN grows at higher temperatures and longer exposure times. Precipitation of Cr_2N is observed after exposure at 600°C for 168h. XPS depth profiles show formation of an outer Fe-oxide layer and an inner (Fe, Cr)-oxide layer. The depletion in chromium observed in the outer oxide layer can be explained by the vaporization of chromium oxide hydroxide in presence of water vapor. Enrichment of manganese is found in the outer oxide layers of the samples exposed at 600°C. Molybdenum, nitrogen and silicon are found in the inner oxide layer at all temperatures. At 600°C for 168h exposure silica particles are observed at the interface of oxide and alloy.

The thickness of the oxide scales formed on nitrided 444 decreases with increasing temperatures. The thickest oxide layer is formed at 500°C for both the exposure times. The thinnest oxide layer is observed at 600°C. According to literature, the higher diffusivity of chromium at higher temperatures can supply more chromium from the substrates toward the oxide and replace the amount loss by vaporization. As already seen, the transfer of nitrogen from the ferritic expanded phase at higher temperatures also influences the oxidation of nitrided 444.

The oxidation rate of nitrided ferritic 444 seems to be lower if compared to the results obtained in previous studies for the nitrided austenitic 304L. The oxides formed are generally smooth but more homogeneous in thickness on the ferritic 444, while areas with thin and thick oxides are observed on the surface of 304L. The different morphologies and growths of the oxides formed can be explained by considering the higher diffusivity of chromium in ferrite than in austenite phase.

Bibliography

[1] W. Frank, G. Hüthwohl and B. Maurer, "*SCR Systems for heavy-duty trucks: progress towards meeting EURO 4 emission standards",* 2005: Performer: PUREM Abgassysteme GmbH and Co., Unna, Germany.

[2] M. Koebel, G. Madia and M. Elsener, "*Selective catalytic reduction of NO and NO_2 at low temperatures",* 2002: Elsevier Science, Catalysis Today, Vol. 73, Number 3, pp. 239-247.

[3] H.L. Fang, H.F. DaCosta, "*Urea thermolysis and NOx reduction with and without SCR catalysts",* 2003: Elsevier B.V, Appl. Catal., Vol. 46, pp. 17-34.

[4] R. Demuzere, "*High alloyed welding products for the urea synthesis process",* 1991: Stainless steel Europe, Vol. 3, Number 9, pp. 55-62.

[5] F.L. LaQue and H.R. Copson, "*Corrosion resistance of metals and alloys",* Second Edition, 1963: Reinhold Publishing Corporation.

[6] A.J. Sedriks, "*Corrosion of stainless steels",* 1979: John Wiley and Sons.

[7] R.M. Davison, *"Corrosion of stainless steels"*, 1987: ASM International, Metals Handbook, Ninth Edition, Corrosion, Vol. 13, pp. 547-565.

[8] R.Y. Chen, W.Y.D. Yuen, "*Review of the high temperature oxidation of iron and carbon steels in air or oxygen",* 2003: Oxidation of Metals, Vol. 59, Issue 5-6, pp 433-468.

[9] Y.L. George, "*High-temperature corrosion: Issues in alloy selection",* 1991: JOM, Vol. 43*,* Number 11, pp. 54-60.

[10] G.E. Totten and M.A.H. Howes, "*Steel Heat Treatment Handbook",* 1997: Marcl Dekker Inc., p. 721.

[11] H. Nii and A Nishimoto, "*Surface modification of ferritic stainless steel by active screen plasma nitring",* 2012: Journal of Physics: Conference Series 379.

[12] D. Pye, "*Pratical Nitriding and Ferritic Nitrocarburizing",* 2003*:* ASM International Materials Park, Ohio, USA.

[13] D.Q. Peng, T.H. Kim, J.H. Chung, J.K. Park, "*Development of nitride-layer of AISI 304 austenitic stainless steel during high-temperature ammonia gas-nitriding",* 2010: Applied Surface Science, Vol. 256, pp. 7522-7529.

[14] M.P. Fewell, J.M. Priest, M.J. Baldwin, G.A. Collins, K.T. Short, "*Nitriding at low temperature",* 2000: Surface and Coating Tecnology, Vol. 131, pp. 284-290.

[15] L.C. Gontijo, R. Machado, L.C. Castelletti, S.E. Kuri, P.A.P. Nascente*, "X-ray diffraction characterization of expanded austenite and ferrite in plasma nitrided stainless steels",* 2010: Surface Engineering, Vol. 26, pp. 265-270.

[16] L.C Gontijo, R. Machado, L.C. Castelletti, S.E. Kuri, P.A.P. Nascente*, "Study of the S Phases Formed on Plasma-Nitrided Austenitic and Ferritic Stainless Steels",* 2010: Materials Science Forum, Vol. 638-642, pp. 775-780.

[17] J.H. Sung, J.H. Kong, D.K. Yoo, H.Y. On, D.J. Lee, H.W. Lee, "*Phase changes of the AISI 430 ferritic stainless steels after high-temperature gas nitriding and tempering heat treatment",* 2007: Materials Science and Engineering, Vol. 489, pp. 38-43.

[18] X. Yun-tao, L. Dao-xin, H. Dong, "*Improvement of erosion and erosion-corrosion resistance of AISI 420 stainless steel by low temperature plasma nitriding",* 2008: Applied Surface Science Vol. 254, pp. 5953-5958.

[19] W. Liang, "*Surface modification of AISI 304 austenitic stainless steel by plasma nitriding",* 2003: Applied Surface Science, Vol. 211, pp. 308-314.

[20] M. Samandi, B.A. Shedden, D.I. Smith, "*Microstructure, corrosion and tribological behaviour of plasma immersion ion-implanted austenitic stainless steel",* 1993: Surface and Coatings Technology, Vol. 59, pp. 261-266.

[21] L. Gil, S. Brühl, L. Jiménez, O. Leon, R. Guevara, M.H. Staia, "*Corrosion performance of the plasma nitrided 316L stainless steel",* 2006: Surface & Coating Tecnology, Vol. 201 pp. 4424-4429.

[22] P. Corengia, G. Ybarra, C. Moina, A. Cabo, E. Broitman, "*Microstructure and corrosion behaviour of DC-pulsed plasma nitrided AISI 410 martensitic stainless steel",* 2004: Surface & Coatings Technology, Vol. 187, pp. 63-69.

[23] C.X. Li and T. Bell, "*A comparative study of low temperature plasma nitriding, carburizing and nitrocarburizing of AISI 410 martensitic stainless steel",* 2007: Materials Science and Technology, Vol. 23, Number 3, pp. 355-361.

[24] A. K. Khanna, *"Introduction to high temperature oxidation and corrosion",* 2002: ASM International.

[25] N. Bertrand, C. Desgranges, D. Poquillon, M.C. Lafont, D. Monceau, "*Iron oxidation at low temperature (260-500°C) in air and the effect of water vapor",* 2010: Oxidation of Metals, Vol. 73, Issue 1-2, pp. 139-162.

[26] A. Rahmel, J. *Tobolski, "Einfluss von wasserdampf und kohlendioxyd auf die oxydation von eisen in sauerstoff bei hohen temperature"*, 1965: Corrosion Science, Vol. 5, p. 333.

[27] M. Thiele, H. Teichmann, W. Schwarz and W. J. Quadakkers, "*Korrosionsverhalten von ferritischen und austenitischen Stählen in simulierten Rauchgasen von Stein und braunkohlebefeuerten Kraftwerken*", 1997: VGB Kraftwerkstechnik Vol. 77, pp. 129-134.

[28] A.S. Khanna, P. Kofstad: Intern. Conf. On Microscopy of Oxidation, Inst. Of Materials, London 1990, UK, p. 113.

[29] S. Jianian, Z. Longjiang, L. Tiefan, *"High-temperature oxidation of Fe-Cr alloys in wet oxygen",* 1997: Oxidation Metals, Vol. 48, Nos. 3/4, pp. 347-356.

[30] G. Hultquist, G. K. Chuah, K. L Tan, *"A sims study of reactions in the metal-oxygen-hydrogen-water system",* 1990: Corrosion Science, Vol. 31, pp. 149-154.

[31] C. S. Tedmon, *"The effect of oxide volatilization on the oxidation kinetics of Cr and Fe-Cr alloys"* 1966: Journal of The Electrochemical Society Vol.113, Issue 8, pp. 766-768.

[32] H. Asteman, J. E. Svensson, L. G. Johansson, M. Norell, "*Indication of chromium oxide hydroxide evaporation during oxidation of 304L at 873 K in the presence of 10% water vapor",* 1999: Oxidation of Metals, Vol 52, Issue 1, pp. 95-111.

[33] H. Asteman, J. E. Svensson, M. Norell, L. G. Johansson, *"Influence of water vapor and flow rate on the high-temperature oxidation of 304L; effect of chromium oxide hydroxide evaporation",* 2000: Oxidation of Metals, Vol. 54, Nos. 1/2, pp. 11-26.

[34] H. Asteman, K. Segerdahl, J. E. Svensson, L. G. Johansson, "*The influence of water vapor on the corrosion of chromia-forming steels",* 2001: Materials Science Forum, Vol. 369-372, pp. 277-286.

[35] H. Asteman, K. Segerdahl, J. E. Svensson, L. G. Johansson, "*Oxidation of stainless steel in H_2O/O_2 environments - Role of chromium evaporation",* 2004: Materials Science Forum, Vol. 461-464, pp. 775-782.

[36] K. Segerdahl, J. E. Svensson, L. G. Johansson, "*The high temperature oxidation of 11% chromium steel: Part I – Influence of pH_2O",* 2002: Materials and Corrosion, Vol. 53, pp. 247-255.

[37] M.P. Brady, J. R. Keiser, K.L. More, M. Fayek, L.R. Walker, R.A. Peascoe-Meisner, L. M. Anovitz, D. J. Wesolowski, D. R. Cole, "*Comparison of short-term oxidation behaviour of model and commercial chromia-forming ferritic stainless steels in dry and wet air",* 2012: Oxidation of Metals, Vol. 78, Issue 1-2, pp. 1-16.

[38] J. Zurek, M. Michalik, F. Schmitz, T.U. Kern, L. Singheiser, W.J. Quadakkers, "*The effect of water-vapor content and gas flow rate on the oxidation mechanism of a 10% Cr-ferritic steel in Ar-H_2O mixtures",* 2005. Oxidation of Metals, Vol. 63, Nos. 5/6, pp. 401-422.

[39] Janvier, 2012, Aperam-Stainless Europe, FT-K44 <*www.aperam.com/stainlesseurope*>.

[40] G.R. Holcomb, D.E. Alman, "*The effect of manganese addictions on the reactive evaporation of chromium in Ni-Cr alloys",* 2006: Scripta Materialia, Vol 54, pp. 1821-1825.

[41] Yu Cao, M. Norell, "*Role of nitrogen uptake in oxidation of 304L and 904L austenitic stainless steels", 2013*: Oxidation of Metals.

[42] Y. Wouters, G. Bamba, A. Galerie, M. Mermoux, J.P. Petit, "*Oxygen and water vapour oxidation of 15Cr ferritic stainless steels with different silicon contents",* 2004: Materials Science Forum, Vols. 461-464, pp. 839-848.

[43] J. Oddershede, T.L. Christiansen, K. Ståhl, M.A.J. Somers, "*Extended X-ray absorption fine structure investigation of nitrogen stabilized expanded austenite",* 2010: Scripta Materialia, Vol. 62, pp. 290-293.

[44] S. Parascandola, W. Möller, "*The nitrogen transport in austenitic stainless steel at moderate temperatures",* 2000: Applied Physics Letters, Vol. 76, Number 16, pp. 2194-2196.

[45] C. Issartel, H. Buscail, Y. Wang, R. Rolland, M. Vilasi, L. Aranda, "*Water vapor effect on ferritic 4509 steel oxidation between 800 and 1000°C",* 2011: Oxidation of Metals, Vol. 76, pp. 127-147.

[46] J. Shu, H. Bi, X. Li, Z. Xu, *"The effects of molybdenum addition on high temperature oxidation behavior at 1000°C of type 444 ferritic stainless steel"*, 2012: Oxidation of Metals, Vol. 78, pp. 253-267.

[47] M.J.G. Vargas, L. Lelait, V. Kolarik, H. Fietzek, M. Juez-Lorenzo, "*The effect of water vapor on the oxidation of stainless steels studied in situ by X-ray diffraction",* 2004: Materials Science Forum, Vols. 461-464, pp. 823-830.

[48] M.H.B. Ani and R. Othman, "*Formation of protective Cr_2O_3 scale at high temperature and the effect of mass transport in the presence of water vapor"*, 2012: Advanced Materials Research, Vol. 402, pp. 412-420.